Oceanologia (2017) 59, 213—237

Available online at www.sciencedirect.com

ScienceDirect

journal homepage: www.journals.elsevier.com/oceanologia/

ORIGINAL RESEARCH ARTICLE

Characterization of the northern Red Sea's oceanic features with remote sensing data and outputs from a global circulation model

Ahmed Eladawy [a,*], Kazuo Nadaoka [b], Abdelazim Negm [a,c], Sommer Abdel-Fattah [a,d], Mahmoud Hanafy [e], Mohamed Shaltout [f,g]

[a] *Department of Environmental Engineering, Egypt-Japan University of Science and Technology, Alexandria, Egypt*
[b] *Department of Transdisciplinary Science and Engineering, School of Environment and Society, Tokyo Institute of Technology, Japan*
[c] *Department of Water and Water Structures Eng., Faculty of Engineering, Zagazig University, Egypt*
[d] *McMaster University, Hamilton, Canada*
[e] *Marine Science Department, Suez Canal University, Faculty of Science, Egypt*
[f] *Oceanography Department, Alexandria University, Faculty of Science, Egypt*
[g] *Marine Science Department, Gothenburg University, Sweden*

Received 23 June 2016; accepted 11 January 2017
Available online 1 February 2017

KEYWORDS
Northern Red Sea;
Remote sensing;
SST fronts;
Atmospheric parameters;
Chlorophyll-*a*;
HYCOM

Summary Sea surface temperature (SST) and surface wind (SW) are considered the most important components in air—sea interactions. This study examines the relationships between SST, SW and various oceanic variables in the northern Red Sea (NRS) during the period of 2000—2014. The current study is the first attempt to identify the SST fronts and their relationship with the dominant circulation patterns. SST fronts are mapped using the Cayula and Cornillon algorithms. The analysis is performed with available remote sensing and reanalyzed data together with 1/12° HYbrid Coordinate Ocean Model (HYCOM) outputs. Seasonal-trend decomposition procedure based on loess (STL) is applied for trend analysis, and Principal Component Analysis (PCA) is run for the atmospheric parameters. The SST, SW speed and Chlorophyll-*a* (Chl-*a*) changes show insignificant trends during the period of 2000—2014. Meridional SST fronts are more significant during the month of January, and fronts that are perpendicular to the sea's axis occur from February to May. Distinct monthly and spatial variations are present in all the examined parameters, although these variations are less pronounced for the wind direction. The SST is mainly controlled by the air

* Corresponding author. Tel.: +20 1005368431; fax: +2 03 4599520.
E-mail address: ahmed.eladawy@ejust.edu.eg (A. Eladawy).
Peer review under the responsibility of Institute of Oceanology of the Polish Academy of Sciences.

Production and hosting by Elsevier

http://dx.doi.org/10.1016/j.oceano.2017.01.002

temperature and sea level pressure. Significant correlations exist between the SST and the studied parameters (alongshore wind stress rather than the cross-shore wind stress, surface circulation, MLD, and Chl-*a*). Surface winds generally flow southeastward parallel to the Red Sea's axis explaining that alongshore wind stress is highly correlated with the studied parameters.

1. Introduction

The Red Sea is a semi-enclosed tropical basin connected to the Indian Ocean through the Bab-al-Mandab Strait. It flows to the Mediterranean Sea through the Suez Canal. The Red Sea supports a rich and diverse ecosystem (Barale and Gade, 2013) and is a unique environment because of the lack of any permanent rivers that flow into it. The Red Sea has an overall negative water balance (i.e. the evaporation is greater than the precipitation and combined river runoff). Although the Red Sea is considered an arid climate region with negligible precipitation and runoff (Al-Horani et al., 2006), flash floods during winter, especially along the eastern coast of the Red Sea, transport terrestrial materials into the NRS. The existence of these flash floods alongside extensive sunlight, clear visibility, deep light penetration, and warm water leads to the extensive development of corals (Al-Rousan et al., 2016). The Red Sea is of special socioeconomic importance because it supports a high volume of shipping activity (Rasul and Stewart, 2015) and other economic activities, including fishing, oil exploration, and tourism. Unfortunately, limited scientific studies have been performed on the Red Sea; a large gap in knowledge exists compared to similar ecosystems (Acker et al., 2008). Thus, the Red Sea is an important area in which a further study of its dynamics would be highly beneficial (Loya et al., 2014).

This study focuses on the descriptive and statistical analysis of physical oceanic characteristics (SST, surface wind, and circulation) over the northern Red Sea (21.5°–30°N, 33.5°–40°E; Fig. 1). Moreover, the relationship between these physical characteristics and Chl-*a* is studied.

SST and SW are considered the most important components in air–sea interactions (Chu, 1989). As such, exploring these two components is the main goal to understand the various dynamics in this region, including the surface circulation, mixed layer depth, upwelling, and Chl-*a* distribution (Gai et al., 2012; Kara et al., 2003; McWilliams et al., 2005; Patzert, 1974; Sofianos and Johns, 2003; Tang et al., 2002).

1.1. Surface wind (SW)

The Red Sea's wind regime is orographically determined due to the existence of high coastal mountain ranges along its eastern and western coasts (Sofianos and Johns, 2007; Sofianos, 2003). The average wind speed generally increases northward (Patzert, 1974). These coastal mountain ranges

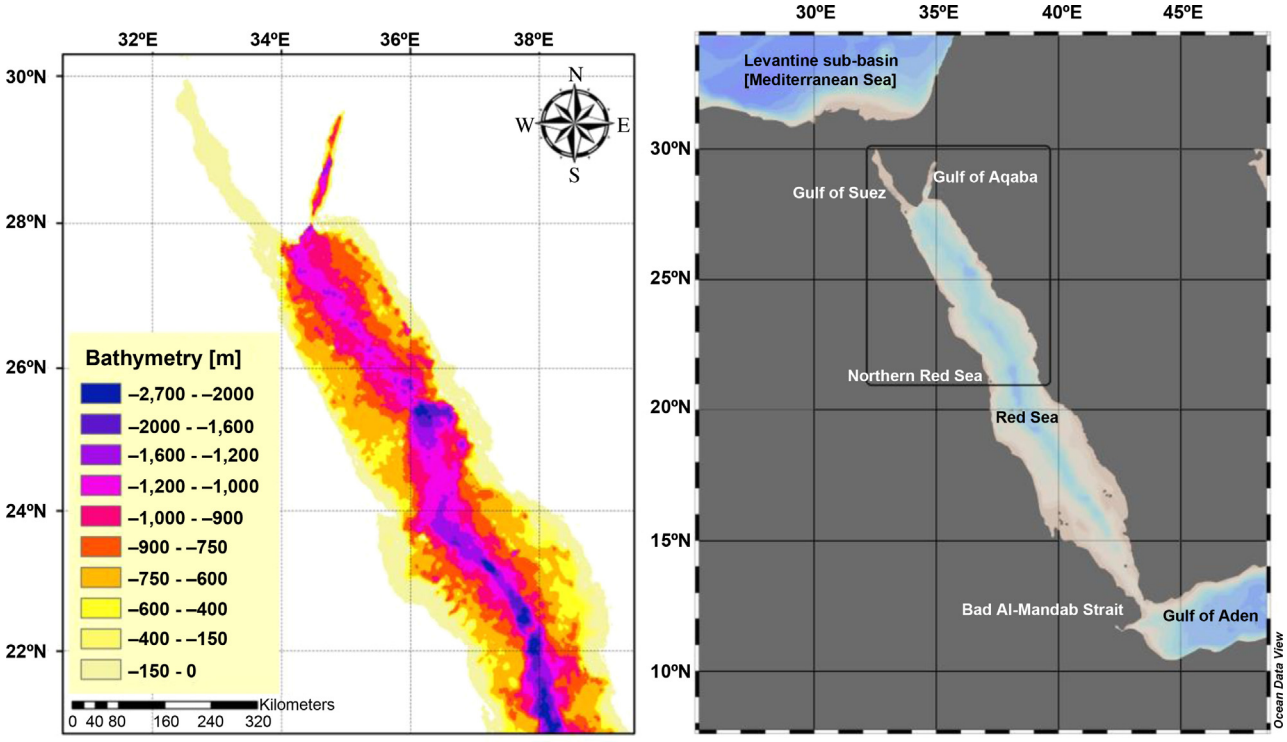

Figure 1 Left: Bathymetric chart of the northern Red Sea (data source: https://www.bodc.ac.uk/products/software_products/gebco_grid_display). Right: Red Sea map. Created from the ocean/world database (available at Arc GIS Online). The black box region represents the study area.

influence the surface wind track to follow the axis of the Red Sea basin (Patzert, 1974). The Red Sea is dominated by northwesterly winds with average speeds between 4 m s^{-1} and 9 m s^{-1} (Bower and Farrar, 2015). The wind system in this region is also influenced by the eastern Mediterranean weather patterns (Pedgley, 1974). A westward-blowing wind stream is present along the northwestern coast of Saudi Arabia during the winter months, which can cause significant evaporation and heat loss along the northeastern Red Sea coast and may drive deep convection (Jiang et al., 2009).

1.2. Sea surface temperature (SST)

According to Morcos (1970), the average annual SST values over the NRS decrease from south to north and from east to west. The Red Sea's seasonal summer to winter SST difference is approximately 6°C (Berman et al., 2003). The annual Red Sea SST during the end of the last century ranged from 22°C to 30°C (Raitsos et al., 2011). The SST over the Red Sea exhibited significant warming from 1997 to 2007 (Raitsos et al., 2011). Raitsos et al. (2011) showed that the SST appeared to follow the air temperatures at 2 m above sea level (T_{2m}) with a 1-month delay. The sea surface temperature is mainly affected by T_{2m}, sea level pressure (*SLP*), precipitation (*P*), total cloud cover (*TCC*), surface wind stress, and air–sea heat fluxes (Shaltout and Omstedt, 2014). Air–sea heat fluxes significantly affect the SST (Shaltout and Omstedt, 2014; Skliris et al., 2012). Shaltout and Omstedt (2014) stated that SST is negatively correlated to *SLP*, *P*, and *TCC* and positively correlated to T_{2m}. If T_{2m} values are higher than the SST, higher (warmer) SST values will be associated with stronger wind stress, while lower (cooler) SST values will be associated with weaker wind stress (Samelson et al., 2006). Conversely, cooler SST values are associated with higher wind stress if the T_{2m} values during winter are cooler than the SST.

1.3. Ocean fronts

Ocean fronts are defined as sharp boundaries between different water masses and are usually accompanied by horizontal gradients of temperature, salinity, density, nutrients and other properties (Belkin and Cornillon, 2003). Surveying of ocean surface thermal fronts can be performed using long-term SST images as was done in the Gulf of Alaska, Bering, Chukchi and Beaufort Seas for 1985–1996 (Belkin et al., 2003). This study applied Cayula–Cornillon algorithms to map the fronts. Temperature fronts tend to develop in the Red Sea because of the extremely high evaporation rate. The northern Red Sea exhibits two main groups of fronts (Belkin and Cornillon, 2007): (1) the Egypt-Saudi Arabia Fronts (ESAF) and (2) the Sudan-Saudi Arabia Fronts (SSAF). Heileman et al. (2008) suggested that remote sensing studies of these fronts are very promising since these fronts have been poorly studied in situ. The current study is the first attempt to identify SST fronts and their relationships with the dominant circulation patterns.

1.4. Circulation patterns and mixed layer depth

Sofianos and Johns (2007) examined the Red Sea circulation pattern and found that the region is characterized by eddies and sub-gyres that are generated by wind forces that vary both spatially and temporally. The Red Sea is also characterized by a very small tidal range (Barale and Gade, 2013). Generally, the basic circulation consists of a cyclonic gyre in the northern Red Sea (Zhai et al., 2015) and a northward-flowing eastern boundary current (Zhai et al., 2015). Eddies throughout the Red Sea have been assessed based on dynamical and statistical approaches (Zhan et al., 2014). Statistics suggested that eddies are generated across the entire Red Sea but are more prevalent in certain regions. A high number of eddies were found in the central basin between 18°N and 24°N. Another study by Zhan et al. (2016) concluded that eddies are most intense during winter, and their strongest activity mainly occurs over the central and northern basins within the uppermost 200 m.

The mixed layer depth (MLD) is the depth at which the temperature or density significantly changes from the surface value, as defined from a standard criterion. The MLD strongly affects the upper ocean physics and the Earth's climate and is considered one of the most recurrent features of the ocean (Falkowski et al., 1998; Pickard and Emery, 1990). Attempts to produce a Red Sea-scale estimation of the MLD have been limited. However, according to Carlson et al. (2014), the MLD in the northern Gulf of Eilat/Aqaba (Red Sea) ranges from less than 50 m during September to more than 350 m during May.

Upwelling is an oceanographic phenomenon by which deeper, usually colder, and nutrient-rich water is brought to the surface to replace the water that has been displaced by coastal or open-ocean winds. Upwelling, which occurs in the open ocean and along the coasts, is significantly controlled by the wind regime (Kahru et al., 2010). Upwelling zones can be identified by cool SSTs and high concentrations of Chl-*a* (Sarhan et al., 2000).

1.5. Chlorophyll-*a*

The surface layer Chl-*a* is considered an indicator of phytoplankton biomass and can be used as an indicator of water quality (Boyer et al., 2009). Chl-*a* concentrations were first mapped on a global scale by the Coastal Zone Color Scanner (CZCS) during the years 1978–1986. This parameter has been continuously mapped since the first operation of the SeaWiFS sensor (1997–2010), with additional data available from the Medium Resolution Imaging Spectrometer (MERIS) (2002–2012) and the Moderate Resolution Imaging Spectroradiometer (MODIS) (2000–present) sensors. The derivation of near-surface Chl-*a* is based on observations of ocean color; algorithms for Chl-*a* retrieval (which can differ between sensors), and regional optimization (Curran et al., 1990; Langodan et al., 2014; Maritorena and O'Reilly, 2000). Acker et al. (2008) analyzed two years of Chl-*a* data; results suggest a different seasonal cycle that consists of a relatively weak northern spring bloom and elevated chlorophyll concentrations to the south (21.5° to 24°N). Slightly higher Chl-*a* concentrations in the NRS are governed by cyclones (Raitsos et al., 2011; Triantafyllou et al., 2014).

Mixed layer depth (MLD) is studied to fully understand the Chl-*a* variability. The surface primary production is highly controlled by the mixed layer depth (Kämpf and Chapman, 2016). Phytoplankton and other organic matter are vertically stirred throughout the surface mixed layer, which indicates

that the MLD influences the relative growth time of such organisms when moving through the euphotic zone (Kämpf and Chapman, 2016).

Upwelling waters are usually rich in dissolved nutrients that are required for phytoplankton growth. These nutrients are transported to surface waters where more sunlight leads to accelerated phytoplankton growth. Conversely, downwelling reduces biological productivity and transports surface water (rich in dissolved materials and dissolved oxygen) and heat to greater depths.

In this study, 15 years of available remote sensing and reanalyzed data, 5 years of 1/12° HYbrid Coordinate Ocean Model (HYCOM) outputs and 2 years of in situ data were analyzed. This enabled (1) an assessment of the applicability of these data over the NRS; (2) an examination of the spatial and temporal variability and trends of the SST and SW as well as mapping of the SST fronts; (3) an examination of the relationship among SST, SW and other physical characteristics (ocean circulation, MLD and upwelling); and (4) a gain in understanding of the spatial and temporal variability of the Chl-*a* concentration, which is highly associated with previously mentioned physical characteristics. The materials and methods are presented in Section 2, the results in Section 3, a discussion in Section 4 and conclusions in Section 5.

2. Material and methods

2.1. Data

The data for this study include the following sources and descriptions for their extractions:

a) Remotely sensed daily ocean wind data were extracted freely from the Advanced Scatterometer (ASCAT) wind maps (Bentamy and Croize-Fillon, 2012) from 2007 to 2014, while historical data (1999–2007) were extracted from the Quick Scatterometer (QUICK SCAT) (Ricciardulli et al., 2011) (ftp://ftp.ifremer.fr/ifremer/cersat/products/gridded/MWF/L3/). The ASCAT data were processed by the National Oceanic and Atmospheric Administration (NOAA), which utilizes measurements from the ASCAT on board the EUMETSAT METOP satellite on the C-band (Chang et al., 2015). These data have a spatial resolution of 0.25° in longitude and latitude.

b) The hourly water temperatures at the Sateya site (25°27.5′N, 34°41.6′E) were measured at a water depth of 5 m from mid-August 2010 to December 31, 2011. The Hurghada Environmental Protection and Conservation Association (HEPCA) installed the temperature logger at Sateya (near Marsa Alam).

c) Remotely sensed daily SST data were extracted freely from NOAA's AVHRR (version 2) over the period of 2000–2014 (ftp://eclipse.ncdc.noaa.gov/pub/OI-daily-v2/NetCDF/). These data have a spatial resolution of 0.25° × 0.25°. The sea surface temperature (SST) from the Advanced Very High-Resolution Radiometer (AVHRR) series onboard NOAA's polar-orbiting satellites has an unbroken, nearly 30-year-long history of observations from the same class of instrument (Casey et al., 2010).

d) Air temperature data at 2 m above sea level (T_{2m}), the sea level pressure (*SLP*), the total precipitation (*TP*), the total cloud cover (*TCC*), and the air–sea heat fluxes were obtained for the period of 2000–2014 from the European Centre for Medium-Range Weather Forecasts (ECMWF); Era-interim full resolution database (http://apps.ecmwf.int/datasets/data/interim-full-daily/levtype=sfc/) with a 3-h temporal resolution and a spatial resolution of 0.125° × 0.125°; these data have been used previously to understand SST dynamics (Dee et al., 2011). Era Interim data were originally on a 0.75° × 0.75° grid size and recently were bi-linearly interpolated to a 0.125° latitude/longitudinal grid to provide a finer resolution (Persson, 2011). This interpolation makes use of land-sea mask to decrease the undesired smoothing of gradients along coastlines, thus Era-interim fine-resolution (0.125°) database was used in the current study.

e) Simulated surface circulation and MLD data were extracted from the 1/12° HYCOM daily output. These data can be freely accessed for the 2010–2014 period from (ftp://ftp.hycom.org/datasets/GLBa0.08/) by using the outputs of experiments (global experiments expt_90.8, expt_90.9, expt_91.0, and expt_91.1). The HYbrid Coordinate Ocean Model (HYCOM) is a community ocean model (http://www.hycom.org) that uses generalized vertical coordinates (Bleck, 2002). The HYCOM is a primitive equation ocean general circulation model that evolved from the Miami Isopycnic-Coordinate Ocean Model (MICOM) (G. R. Halliwell, 2004b). The HYCOM is configured on a Mercator grid between 78°S and 47°N with 32 vertical layers. The HYCOM uses a quality-controlled NRL DBDB2 dataset to prepare the bathymetry and the NAVy Global Environmental Model (NAVGEM) version 1.2 to prepare the surface forcing files, including the wind stress, wind speed, heat flux (bulk formula), and precipitation (https://hycom.org/data/glba0pt08/expt-91pt0#blkdat.input).

f) Actual observation data (Boyer et al., 2013) for the vertical distributions of the temperature and salinity over the NRS are freely available via http://www.nodc.noaa.gov/OC5/WOD/datageo.html. The CTD profiles cover the period from 1977 to 2014 at specific locations across the northern Red Sea were acquired.

g) Remotely sensed Chl-*a* data (Ocean Biology Processing Group, 2003) were extracted from NASA's Aqua satellite via the MODIS (Moderate Resolution Imaging Spectroradiometer) sensor. We used the Level 3 standard mapped image (SMI) chlorophyll-*a* dataset (hereafter MODIS_L3_Chl-*a*), which has a daily temporal resolution and 4.6 km (at the equator) spatial resolution (https://oceandata.sci.gsfc.nasa.gov/MODIS-Aqua/Mapped/Daily/4km).

2.2. Methodology

This analysis used data from remote sensing and reanalyzed data over a 15-year period (2000–2014). In addition, the 1/12° global HYCOM output results over the last 5-year period (2010–2014) were used to examine the spatial and temporal characteristics of the surface wind stress, sea surface temperature dynamics, and their effects on different features of the northern Red Sea.

Generally, seasonal-trend decomposition procedure based on loess (STL; Cleveland et al., 1990) is applied to resolve the

seasonality and trends in long-term SW data. This procedure was chosen because it provides an accurate assessment of nonlinear trends to avoid any biases controlled by single values (Shamsudduha et al., 2009). In addition, STL can efficiently handle any type of seasonality. The equation that represents the STL method was integrated into the applied R statistical language as follows:

$$VM_t = T_t + S_t + R_t, \quad (1)$$

where VM_t is the variable magnitude at time 't', T_t is the trend component, S_t is the seasonal component, and R_t is the residual component.

The relationship between any two variables is considered a significant dependency only when their correlation is significant at a 95% confidence level. Principle component analysis (PCA) was used to confirm the dependency between several variables. PCA is a technique that transforms a set of correlated variables into a set of uncorrelated factors (Abdi and Williams, 2010; Wold et al., 1987). The goal of PCA is to represent data as a new set of new orthogonal variables (principal components) while attempting to preserve the relationships in the original data (Ouyang, 2005). The principal components are ordered based on their variance in descending order. The total variation that is explained by the principal components to the current component is named the cumulative proportion. PCA was applied to the rainfall, *SLP*, and SST fields to identify their characteristic variability patterns (Giannini et al., 2000). In this study, this method allows for the determination of the covariability patterns of each of the primary meteorological fields (*SLP* and SST) with the dependent field (rainfall).

2.2.1. Surface wind

Monthly distributions of remotely sensed surface wind speed data (ASCAT and QUICKSCAT data) and the monthly dominant surface wind direction were used in this study. These data have been used to understand the effect of the wind on the ocean physics, where τ_x and τ_y denote the eastward and northward wind stress components, respectively, which are calculated with a standard bulk formulation:

$$\tau\,(\text{wind stress}) = \sqrt{\tau_x^2 + \tau_y^2}, \quad (2)$$

$$\tau_x = \rho_a C_D U W, \quad (3)$$

$$\tau_y = \rho_a C_D V W. \quad (4)$$

W is the surface wind speed (nominally at 10-m height), U (V) is the zonal (meridional) wind speed at 10-m height and ρ_a (=1.3 kg m^{-3}) is the air density. C_D is the air drag coefficient, which was calculated in its non-linear form (Large and Pond, 1981) and modified for low wind speeds as in Trenberth et al. (1990):

$$\begin{aligned} C_D &= 0.00218 && \text{for } W = 1\,\text{m s}^{-1},\\ C_D &= (0.62 + 1.56/W)\,0.001 && \text{for } 1\,\text{m s}^{-1} < W = 3\,\text{m s}^{-1},\\ C_D &= 0.00114 && \text{for } 3\,\text{m s}^{-1} < W = 10\,\text{m s}^{-1},\\ C_D &= (0.49 + 0.065\,W)\,0.001 && \text{for } W > 10\,\text{m s}^{-1}. \end{aligned} \quad (5)$$

The surface wind stress components were rotated 30° anti-clockwise from the XY-coordinate plane because of the Red Sea's alignment to determine the effect of the surface wind stress on the SST. Thus, the wind stress components became cross-shore (τ_{cr}) and alongshore (τ_{al}) to the coast.

2.2.2. Sea surface temperature dynamics

The STL procedure was applied to the SST data, as described in the SW section. The spatial and temporal distributions of the NRS SSTs from NOAA's AVHRR database were studied by analyzing the monthly average distributions. These data have been used to understand the seasonal SST variability over the NRS in addition to monitoring SST fronts. The amplitude and phase angle of the annual SST cycle were calculated for each grid (Shaltout and Omstedt, 2014). The daily SST at each grid (i, j) was analyzed by using Fourier analyses of a periodic function:

$$f_{i,j}(t) = a_{0,i,j} + \sum_{n=1}^{N}\left\{a_{n,i,j}\cos\left(\frac{2\pi nt}{T}\right) + b_{n,i,j}\sin\left(\frac{2\pi nt}{T}\right)\right\}, \quad (6)$$

where a_n and b_n are the Fourier coefficients, T is the one-year period, and t is the time. When the seasonal cycle is predominant, only the terms up to n = 1 can be retained:

$$\begin{aligned} f_{i,j}(t) &= a_{0,i,j} + a_{i,j}\cos\left(\frac{2\pi t}{T}\right) + b_{i,j}\sin\left(\frac{2\pi t}{T}\right)\\ &= a_{0,i,j} + A_{i,j}\cos\left(\frac{2\pi t}{T} + \vartheta_{i,j}\right), \end{aligned} \quad (7)$$

where the subscript n = 1 is not indicated, and the amplitude A and the phase angle ϑ are defined as follows:

$$A = \sqrt{a^2 + b^2}, \quad \vartheta = \tan^{-1}\frac{b}{a}. \quad (8)$$

The amplitude and phase angle were calculated to examine the SST's seasonality and the thermal effect on the surface circulation pattern (Marullo et al., 1999; Shaltout and Omstedt, 2014).

SST fronts were calculated to distinguish the processes in the ocean and were defined as the boundaries between different water masses. SST fronts may be associated with strong currents or significant upwelling. SST fronts were calculated by using the Cayula and Cornillon algorithms (Cayula and Cornillon, 1992). The Cayula–Cornillon single-image algorithm is currently integrated into the Marine Geospatial Ecology Tools (MGET) (Roberts et al., 2010). The Cayula and Cornillon algorithm combined with the ArcGIS 10.3 software was performed to map the SST on a monthly basis. The algorithm begins with deleting any invalid pixels (i.e., land pixels) within each single raster data. Then, the algorithm uses a 3 × 3 moving window as a median filter for all the grids. Afterward, using a 32 × 32 moving window which has a stride of 16 pixels (i.e. 16 pixels per step), the program identifies the windows that exhibit a bimodal distribution by running a histogram analysis. The grids are separated into two populations according to the optimal separation value. The SST fronts are described by the adjacent grids between the two populations.

Generally, the monthly and inter-annual effects of various atmospheric parameters on the SST variability (ERA-Interim reanalysis), i.e., T_{2m}, *SLP*, *P*, *TCC*, wind stress and air–sea heat fluxes, were studied by using a correlation analysis between these parameters. All the correlation coefficients

were tested for significance at the 95% level. PCA was performed for the atmospheric data, including *SLP*, *TP*, *TCC*, τ_{cr}, τ_{al}, T_{2m}, F_n and F_s^o, to confirm the dependency between the studied parameters.

2.2.3. HYCOM vertical velocity and upwelling

The interaction among the SST, τ_{cr}, and τ_{al} on the studied MLD and Chl-*a* were investigated by using direct correlation coefficient methods.

The effects of the SST and SW on the vertical velocity were examined by calculating the correlation between the surface stratification (density difference across the MLD from the independent database), τ_{cr} and τ_{al} and the surface HYCOM's vertical velocity (hereafter HYCOM_ω). The HYCOM's archives do not contain HYCOM_ω. Thus, HYCOM_ω was calculated by vertically integrating the continuity equation in Cartesian coordinates (Halliwell, 2004a,b). HYCOM_ω across the intermediate layer (between the bottom of the mixed layer depth and the top of bottom layer) was identified.

3. Results

The remotely sensed data were compared to the measured water temperature during the same measurement period to assess the accuracy of the SST data from NOAA's AVHRR. The

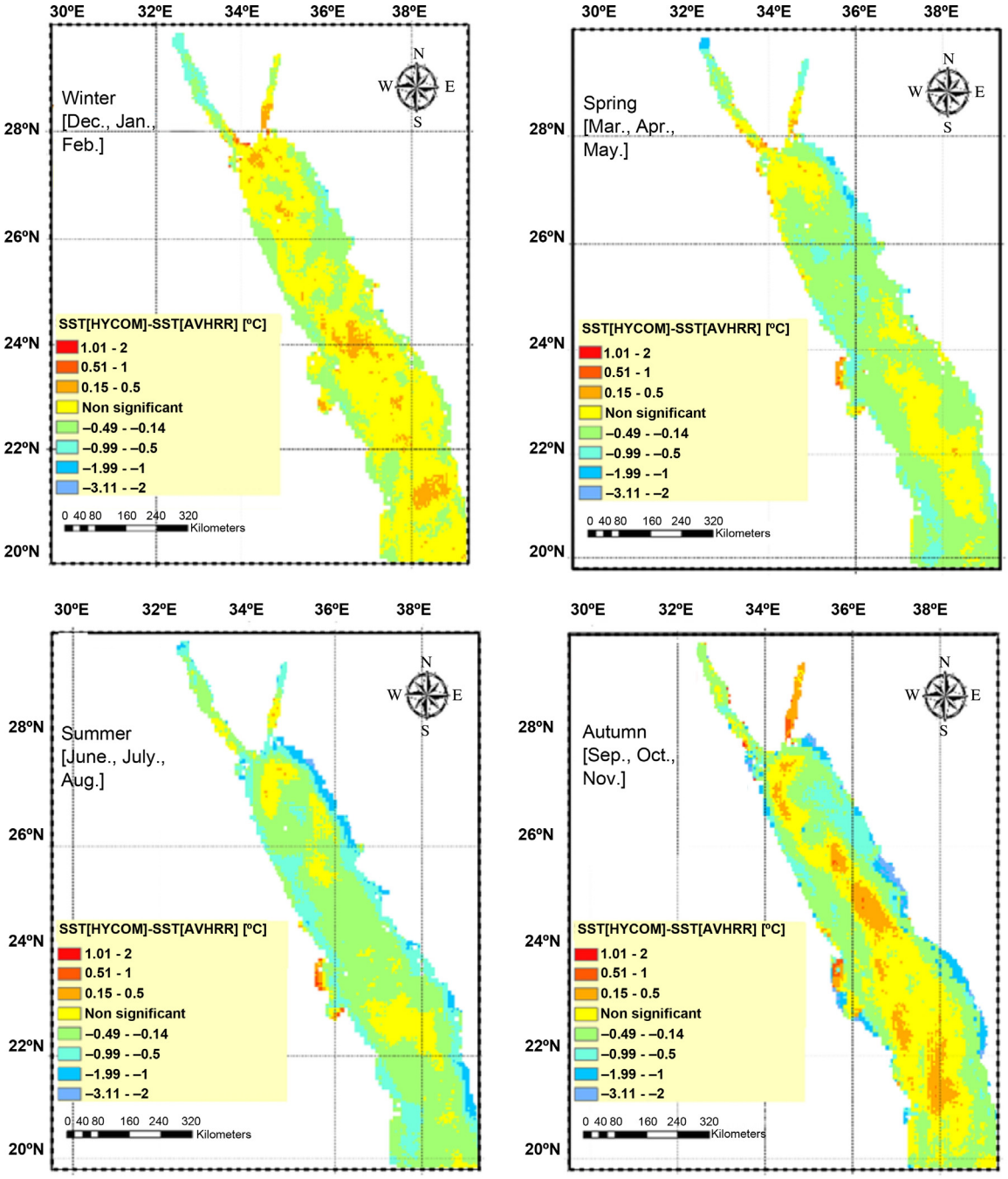

Figure 2 Seasonal bias between the HYCOM's SST and the AVHRR's SST during 2010–2014.

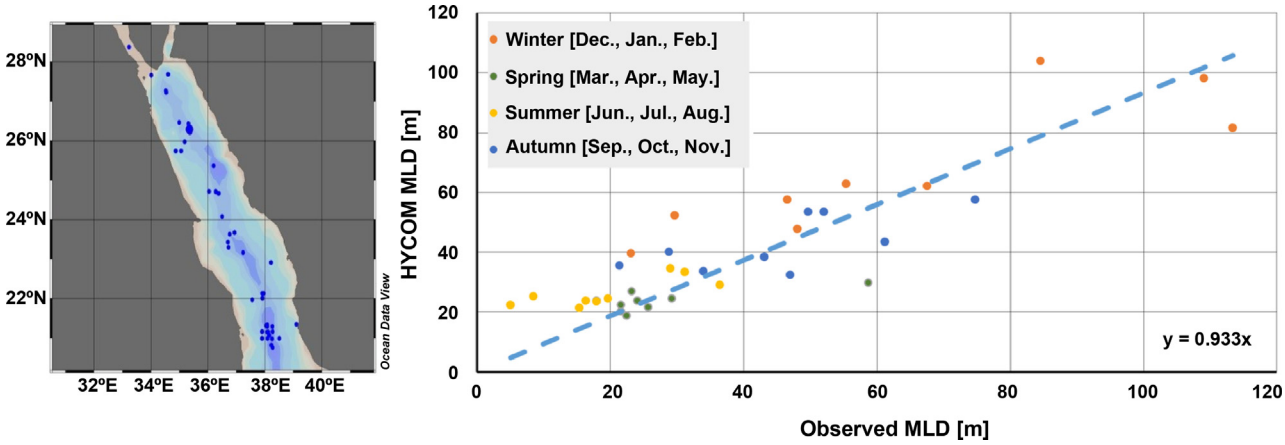

Figure 3 Correlation between the HYCOM's MLD and the observed MLD (shown in the map) during 2010–2014 (R^2 = 0.7697).

temperatures from the surface to a depth of 5 m for the in situ data were assumed to be constant, although slight differences were likely to occur between the actual SST (surface temperature) and measured water temperature. The daily AVHRR SST matched the measured SST (correlation coefficient R = 0.97, root mean square error = 0.57°C, and n = 2813).

The daily AVHRR SST and HYCOM SST showed a spatially significant correlation that ranged from R = 0.84 during autumn months to R = 0.91 during spring months from 2010 to 2014 (number of observations n = 1826). The difference between the AVHRR SST and HYCOM SST was insignificant over 93% of the area of the northern Red Sea. The daily HYCOM SST gave approximately 0.3°C overestimation compared to the AVHRR SST over 6% of the study area, which was most prominent during cold seasons. The daily HYCOM SST over the coastal area illustrated approximately 1°C underestimation compared to the AVHRR SST, which was most pronounced during autumn and along the eastern coast (Fig. 2).

The MLD was calculated based on the available measured temperature and salinity profiles (36 profiles) through a chosen temperature criterion of a 0.2°C absolute difference from a reference depth of 10 m. The reference depth was set to 10 m to avoid a large portion of the strong diurnal cycle in the top few meters of the ocean (De Boyer Montégut et al., 2004). The HYCOM MLD and observed MLD showed a significant correlation (Fig. 3) that ranged from winter (R = 0.86, n = 9) to spring (R = 0.70, n = 9). The HYCOM MLD and observed MLD showed insignificant bias over 27% of the available profiles. Moreover, the HYCOM MLD showed an overestimation (underestimation) compared to the observed MLDs over 43% (30%) of the available profiles by an average value of 13 m (10 m). The approximate uncertainty of 10 m is small compared to the total depth. Thus, the 1/12° HYCOM's daily outputs proved to be a relevant tool for the current study.

MODIS_L3_Chl-*a* is the most widely used product from ocean color data (Carder et al., 2004). The MODIS_L3_Chl-*a* values matched the in situ data, as reported by Clerici et al. (2008): the Chl-*a* values ranged from 0.1 to 1.0 $\mu g\ L^{-1}$, and the agreement between the in situ measured values and remote sensing values was very good, with a bias (δ) as low as −0.021, a limited root-mean-square deviation (RMSD (Δ) = 0.182) and a high determination coefficient (r^2 = 0.805). Another study (Brewin et al., 2013) utilized eighty-five chlorophyll observations and were matched to MODIS-Aqua satellite remote sensing reflectance (Rrs) data. This study concluded that the precision and accuracy of the standard NASA algorithm in the oligotrophic waters of the Red Sea were found to be comparable with other areas in the global ocean.

3.1. Scatterometer surface wind

The sea level pressure was studied over a larger domain (29–46°E; 13–34°N) to better understand the NRS surface wind system. Isobars (lines of equal sea level pressure)

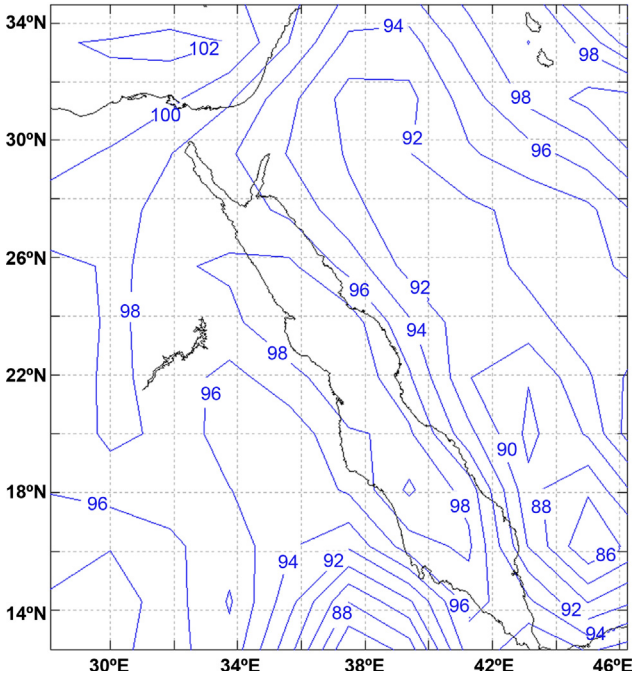

Figure 4 Long-term mean of the surface pressure [KPascals] over the NRS. The climatology was processed from the source data: Monthly NCEP/DOE Reanalysis Surface_gauss_clima.

showed a parallel line to the longitudinal axis of the Red Sea most of the year (Fig. 4), partly because of the effect of the high mountains on both sides of the NRS. The sea level pressure decreased from higher values over the Levantine Basin (southeastern basin of the Mediterranean Sea) to minimum values over the Gulf of Aden to the south. The surface wind was roughly parallel to the isobars in a clockwise direction around high-pressure areas because of the balance among the pressure gradient force, centrifugal force and Coriolis force. This result indicates that the geostrophic wind direction over the NRS blew toward the southeast and was parallel to the Red Sea axis. Moreover, the sea level pressure patterns over the NRS showed a smooth pattern, which decreased the wind speed. The general atmospheric circulation over the Red sea favored the transfer of warm and moist air masses from the southern Red Sea Basin (Abualnaja et al., 2015; Papadopoulos et al., 2013). The combined effect of weak winds with warm and moist air decreased the heat loss.

The surface wind speed (Figs. 5 and 6) over the NRS ranged between 4 m s^{-1} (most significantly during July and April, especially over the southwestern area of the NRS) and 8.9 m s^{-1} (most significantly during September, especially over the northwestern area of the NRS). This result matches previous findings (Bower and Farrar, 2015; Patzert, 1974). After using linear regression for trend analysis, the SW magnitude showed a significant decreasing trend of −0.198 m s^{-1} $decade^{-1}$ during the study period; the time series data were dominated by the first year of the analysis (2000) (6.7 m s^{-1}). Despite the widespread application of linear regression for trend analysis, we attempted to test STL to provide accurate assessments of the nonlinear trends. A representative STL decomposition (for the NRS average SW speed, shown in Fig. 6b and c) was performed to obtain a complete picture of the SW speed time series. Unlike trend analysis via linear regression, this STL analysis showed the insignificant trend and constant seasonality. The time series of the spatially averaged wind speed over the NRS showed a significant annual averaged SW variation over the NRS that ranged from 6.7 m s^{-1} in 2000 to 5.7 m s^{-1} in 2003. In addition, a less significant SW monthly cycle occurred that ranged from maximum values (6.74 m s^{-1}) in September to minimum values in July (4.99 m s^{-1}). Generally, the predominant wind direction in the NRS followed the sea level pressure system and blew parallel to the Red Sea's axis from the northwesterly direction most of the year (Fig. 5). This result supports the previous findings of Patzert (1974) and Rao and Behairy (1986). The SW speed from October to December over the southern portion of the NRS slightly deviated to the southwest direction. During hotter months (May–September), the wind direction over the southern area of the NRS was continuous and flowed parallel to the Red Sea axis. The month of January showed high variability in the daily surface wind direction. Three daily wind systems described the surface wind over the NRS area: the wind that blew parallel to the Red Sea axis from the northwesterly direction (predominant direction), north-blowing wind-stream bands along the northwestern Saudi Arabian coast, and eastward-blowing wind over the northern NRS. The last two wind systems

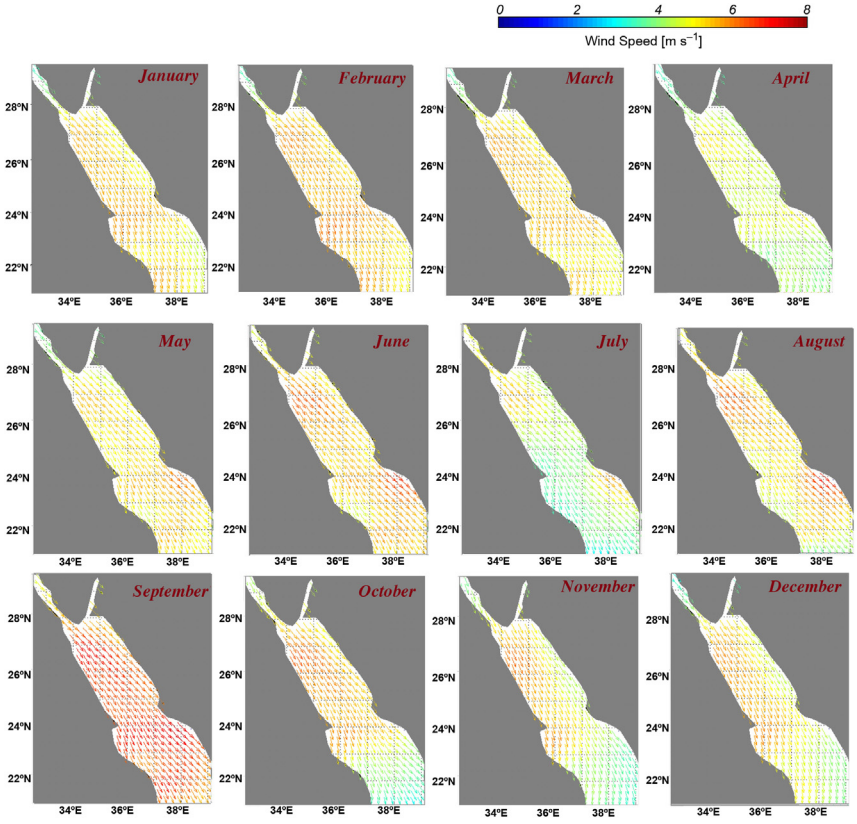

Figure 5 Spatially averaged monthly sea surface wind speed [m s^{-1}] and the predominant monthly wind direction.

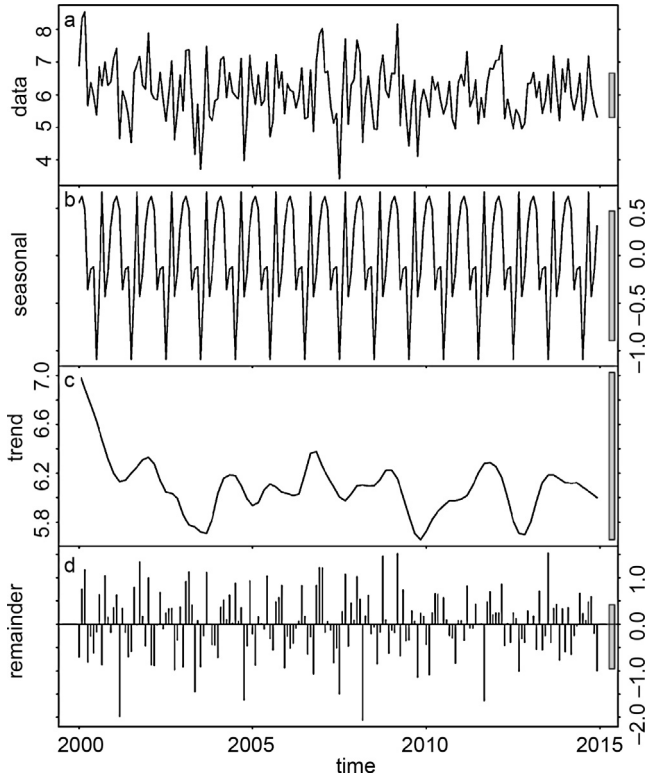

Figure 6 STL decomposition of the average SW speed time-series data [m s^{-1}] for the NRS. The original time series of the average monthly data are shown in (a). The seasonal and trend components that were decomposed from the time series by STL are shown in (b) and (c). The residual component of the time series is shown in (d). The bars on the right-hand ends of the plots provide a comparison of the vertical scales.

occurred on two or three days in January and had a relatively small contribution to the monthly mean surface wind stress.

3.2. AVHRR sea surface temperature

The NRS SST ranged from 22°C (most significantly during March over the northwestern area) to 32°C (most noticeably during August over the southeastern area), as shown in Fig. 7. The NRS showed an increasing SST pattern from northwest to southeast because of the effects of the surface wind regime (Rao and Behairy, 1986), surface thermohaline cyclonic circulation (Sofianos and Johns, 2003) and total heat loss from the atmosphere (Abualnaja et al., 2015; Omstedt, 2011). The existence of high SST values along the eastern boundary of the NRS suggests the presence of an eastern boundary current that carries warm water from the south to the north. The spreading of cold water southward from the northward corner suggests that the eastern boundary current turns southward in the northern NRS and feeds the western boundary current.

The sea surface temperature fronts (Fig. 7) showed a barrier between two water masses that was most pronounced in December, January, and February. The NRS showed clear SST meridional fronts from November to February and became more significant in January. These meridional fronts are classified as the Egypt-Saudi Arabia Fronts (ESAF) because of their occurrence between the two countries, which agrees with Heileman and Mistafa's (2008) study. Zonal fronts that were perpendicular to the Sea axis occurred from March to May. Fronts with lower frequency occurred parallel to the Red Sea axis from June to September, which indicates that the NRS SST showed gentle meridional patterns. The frequency of the NRS fronts lessened dramatically during October. Moreover, coastal fronts most prominently appeared along the eastern coasts during warm seasons, which matches the findings of Blythe et al. (2011). Fronts along the eastern coasts during warm seasons are classified as warm fronts (colder in-shore), which can be explained by the dominant northwesterly wind over the NRS. Generally, the locations of the NRS open water fronts were clearly associated with a tongue of warm water along the eastern coasts.

Time series of spatially averaged monthly SST over the NRS (Fig. 8a) showed that the SST monthly variation was associated with the T_{2m}; the T_{2m} annual cycle was more significant than the SST annual cycle. The positive difference (SST − T_{2m}) indicated sensible heat transport from the NRS to the atmosphere (the summer T_{2m} was warmer than the SST by approximately 2°C, while the opposite occurred during winter, as seen in Fig. 9a). The difference reached 5°C, particularly during winter. The annual SST over the NRS ranged from 26.57°C in 2000 to 27.12°C in 2009. During 2010, the annual average SST was the highest with 27.7°C. On the other hand, T_{2m} ranged from 27.15°C in 2011 to 27.67°C in 2014. Similarly, the annual average T_{2m} in 2010 was 28.2°C, which was an anomaly (much higher than the climatological mean). During the summer of 2010, a major coral bleaching event was recorded in the central Red Sea (Furby et al., 2013) and was the same year as the highest annual SST that was recorded over the NRS during the last 15 years (Furby et al., 2013). Trend analysis that was based on linear regression indicated that the SST exhibited a significant increasing trend of 0.3°C decade^{-1} over the study period, which was dominated by the odd event in 2010. Fig. 8b represents an STL decomposition of the average SST time-series data [°C] for the NRS. The original time series of the average monthly data are shown in (i), and the seasonal and trend components that were decomposed from the time series by STL are shown in (ii) and (iii). The residual component of the time series is shown in (iv). Nearly constant seasonality and slight increasing trends in the time series data of the SST can be observed, especially over the last five years. The results from the STL method agree with the findings from the linear regression trend analysis but allow a more flexible representation of the underlying trend.

Fourier analysis of daily SST data for these 15 years of data indicated that the most significant SST cycle was the annual cycle ($n = 1$) over the entire NRS. Significant annual cycle variability was present in the Red Sea SST, which usually attained its minimum amplitude (2.68°C) in the south and its maximum amplitude (5°C) in the Gulf of Suez (Fig. 9a). Over the Gulf of Suez, the SST seasonality amplitude was approximately 1°C larger than that in the rest of the NRS, partly because of the shallow water characteristics of the Gulf of Suez. In addition, the SST seasonality amplitude over the Gulf of Aqaba was much lower than that over the Gulf of Suez (by 1°C), which suggests that the MLD over the Gulf of Aqaba was much deeper than that over the Gulf of Suez. Moreover, the Red Sea SST seasonality phase lag (Fig. 9b) describes a

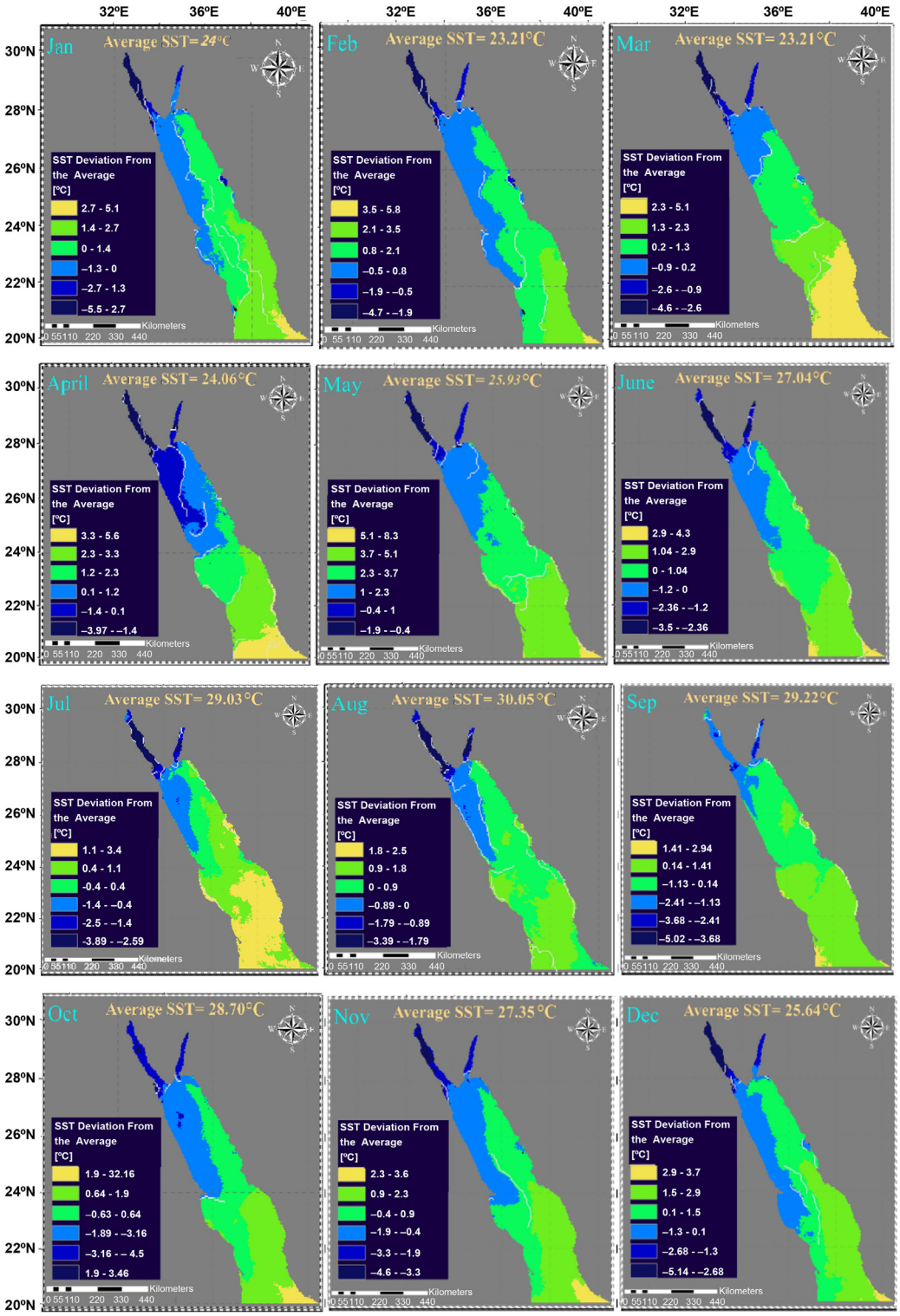

Figure 7 Climatology of the AVHRR's SST (2000–2014) on the northern Red Sea. The solid white line describes the sea surface temperature fronts (the color legend differs between figures).

meridional gradient from a minimum value of 32 days over the southeastern area to a maximum value of 43 days over the central-western area of the NRS; this indicates that seasons arrived earlier in the central-eastern area than in the western area of the NRS. In addition, the SST seasonality phase over the Gulf of Suez decreased from north to south, independent from the rest of the NRS.

Fig. 10 shows the spatial distribution of the correlation coefficient between the Red Sea SST and oceanic/weather parameters. Generally, a significant negative correlation

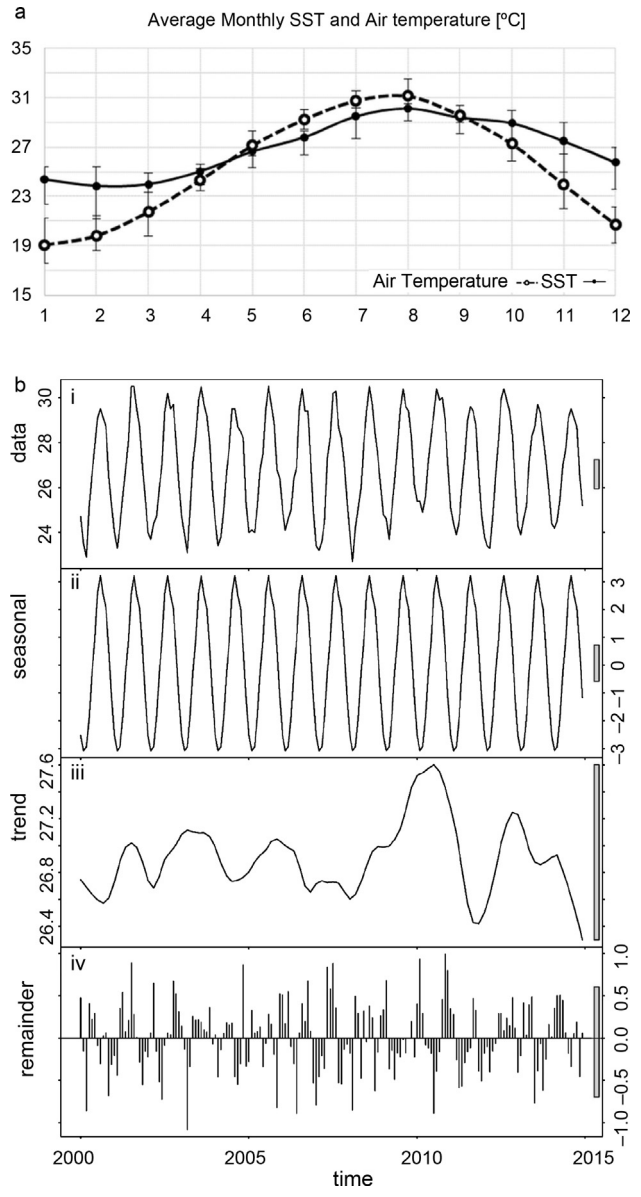

Figure 8 (a) Average monthly SST (air temperature) in the NRS from the AVHRR (ECMWF) data (2000–2014); (b) STL decomposition of the average SST time-series data [°C] for the NRS.

existed between the SST and the atmospheric parameters, including the *SLP*, net heat loss from the sea (F_n), and *TCC*, and a positive correlation between the SST and T_{2m}, τ_{al} and solar radiation to the open water surface (F_s^o). Moreover, a non-significant correlation exists between the SST and the atmospheric parameters TP and τ_{cr}. The SST has a strong positive correlation with the T_{2m}. Moreover, the influence of τ_{al} on the SST is much larger than the effect on τ_{cr}, partly because of the dominant northwesterly winds over the NRS. Table 1 shows the monthly correlation coefficients between SST and the studied atmospheric components over the study area (n = 180, the level of significance = 95%); the percentage of the study area that was significantly correlated with the studied atmospheric components is shown. Based on the results, T_{2m} significantly affected the SST over the entire NRS mostly throughout the year but only over 71% of the area during winter. On the other hand, SST was significantly affected by the alongshore wind stress during cold seasons compared to other seasons. Because this area is dry, *TP* has a relatively less significant effect, only over 31% of the area during winter. The net heat loss from the sea (F_n) widely affected the SST during autumn. On the other hand, the solar radiation on the open water surface (F_s^o; negative fluxes indicate fluxes into the water body) had seasonal characteristics and thus more greatly affected SST during spring and autumn compared to during summer and winter. The annual correlations between SST and the studied parameters, including the *SLP*, *TP*, *TCC*, τ_{cr}, τ_{al}, T_{2m}, F_n and F_s^o, were significant over 100%, 2%, 75%, 12%, 88%, 100%, 95% and 43% of the study area, respectively.

Multiple regression analyses (n = 5479) showed that T_{2m}, *SLP*, and F_n can explain 94.68% of the general SST characteristics over the NRS with a 0.755°C standard error. However, all the studied parameters, including, the *SLP*, *TP*, *TCC*, τ_{cr}, τ_{al}, T_{2m}, F_n and F_s^o, can explain 96.12% of the general SST characteristics over the NRS with a 0.6506°C standard error. Thus, considering the effect of T_{2m}, *SLP* and F_n is sufficient to study the general SST variation over the NRS; however, the effect of water exchange with the southern Red Sea sub-basin and the effect of the NRS circulation should be considered to study the local features of the NRS SST.

Moreover, principal component analysis (PCA) was run for the atmospheric data, including the *SLP*, *TP*, *TCC*, τ_{cr}, τ_{al}, T_{2m}, F_n and F_s^o (Table 2). The results showed that 90% of the overall variance was explained by the first five principal components and 58.6% by only the first two principal components. The first component (PC1, 40.0% of the overall variance) was dominated by the SST, T_{2m}, and *SLP*. The second component (PC2, 19% of the overall variance) was dominated by F_s^o. The third component (PC3, 13% of the overall variance) was related to the wind stress components (τ_{cr} and τ_{al}). Moreover, the fifth component (PC5, 9% of the overall variance) was related to *TP* and *TCC*. Statistical analysis was performed using R programming language (R-3.3.0).

3.3. HYCOM surface circulation

The NRS surface circulation showed a distinct monthly variation with opposite regimes (Fig. 11). From July to December, the surface circulation was characterized by an eastern boundary current that was directed toward the north, which was responsible for the warm tongue along the eastern coast (supporting the current findings from the AVHRR's SST analyses). The eastern boundary current turned southward and fed the western boundary current, forming the NRS cyclonic circulation, which was partly responsible for the cold water that was advected southward from the northward corner along the western coasts (supporting the current findings from the AVHRR's SST analyses). These results agree with those of Sofianos (2003) and Yao et al. (2014).

From July to September, the circulation was characterized by two cyclonic gyres. One of these gyres appeared over the northern area and the other over the southern area. This observation suggests a sudden change in the MLD at the interface between the two gyres. During October and November, the two gyres merged into one unified gyre. One northern cyclonic gyre appeared during December and January. An anti-cyclonic eddy that was centered at 27°N was present during March, April, and May, which cooled this area. In

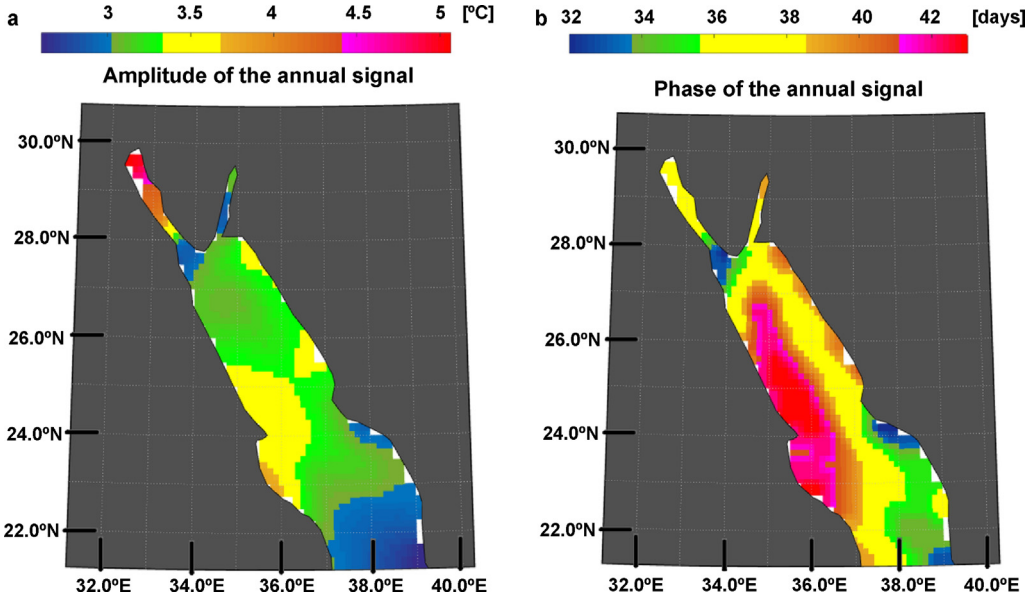

Figure 9 Spatial distribution of the amplitude (a) and phase (b) of the annual SST in the Red Sea (2000–2014).

December and January, a well-structured cyclonic gyre appeared over the northern portion of the study area, which suggests significant vertical motion. February and June, which were transition periods, were characterized by cross-basin circulation, which supports the previous findings of Sofianos and Johns (2003) and Sofianos et al. (2002). Over the Gulfs of Suez and Aqaba, the current was mostly directed southward to deeper portions of the Red Sea, which suggests that the general surface circulation of the Red Sea did not significantly affect the water in the two gulfs. The SST seasonality phase and the surface current distributions showed zonal patterns, which indicates that the surface circulation was significantly correlated with the SST, especially during December and January.

3.4. HYCOM mixed layer depth

The HYCOM monthly average MLD values showed significant monthly variation (Fig. 12). The HYCOM MLD reached extreme values, which ranged from approximately 650 m during March to approximately 63 m during September and October, most significantly over the Gulf of Aqaba. This result agrees with those of Genin et al. (1995) and Labiosa et al. (2003). In addition, the higher HYCOM MLD values over the Gulf of Aqaba during cold months can be explained by extensive winter mixing (Lindell and Post, 1995).

The HYCOM MLD values were lower during warmer months than during colder months by approximately 20%. The HYCOM MLD was lowest with 64 m and 55 m, respectively along the northwestern coast during May and June, while the HYCOM MLD was lowest with 56 m and 50 m, respectively over the southeastern area during July and August. This result can be explained by extensive wind mixing: higher wind speed occurred over the northwestern NRS during May and June, as seen in Fig. 4.

The monthly correlations between the MLD and the studied parameters, including SST, τ_{cr}, and τ_{al}, were significant over 50%, 2% and 42% of the study area, respectively (Fig. 13), which indicates the importance of SST and τ_{al} in studying the MLD. The SST was negatively correlated with the HYCOM MLD and was most pronounced over the central portion of the study area the Gulf of Aqaba. In addition, τ_{al} was negatively correlated with the HYCOM MLD and was most pronounced over the Gulf of Aqaba and Gulf of Suez.

The correlation coefficient was calculated after removing the seasonal cycle to examine whether the correlation between SST and MLD depended on a seasonal cycle. The correlation coefficient between SST and MLD showed no significant difference before and after the removal of the seasonal cycle, which indicates that the correlation coefficient did not depend on a seasonal cycle.

Density profiles at 11 points (Fig. 14) were calculated based on the HYCOM results for 2014 to investigate the hydrographic conditions of the NRS. Density profiles at a point in the middle of the Gulf of Suez showed that the Gulf water was well mixed throughout the year. The profiles of the Gulf of Aqaba hydrography exhibited strong seasonal variability, with deep mixing from December to June and stable stratification afterward. The remaining 9 points were distributed in the eastern, middle and western portions of the remainder of the NRS. W1, M1, and E1 nearly had the same hydrographic characteristics throughout the year. The layers within the first 200 m were very well mixed in the months prior to May. Stratification appeared from May until December. To the south, the profiles indicated stable stratification throughout the year, which was most significant from July to October.

3.5. HYCOM vertical velocity (HYCOM_ω)

The HYCOM vertical velocity within the intermediate layer (the intermediate layer lies between the bottom of the mixed layer depth and the top of the bottom layer where the sea water density changes rapidly with depth) exhibited an annual spatial variation from −0.1 to 0.04 cm s^{-1} over the NRS (Fig. 15). Permanent upwelling events comprised

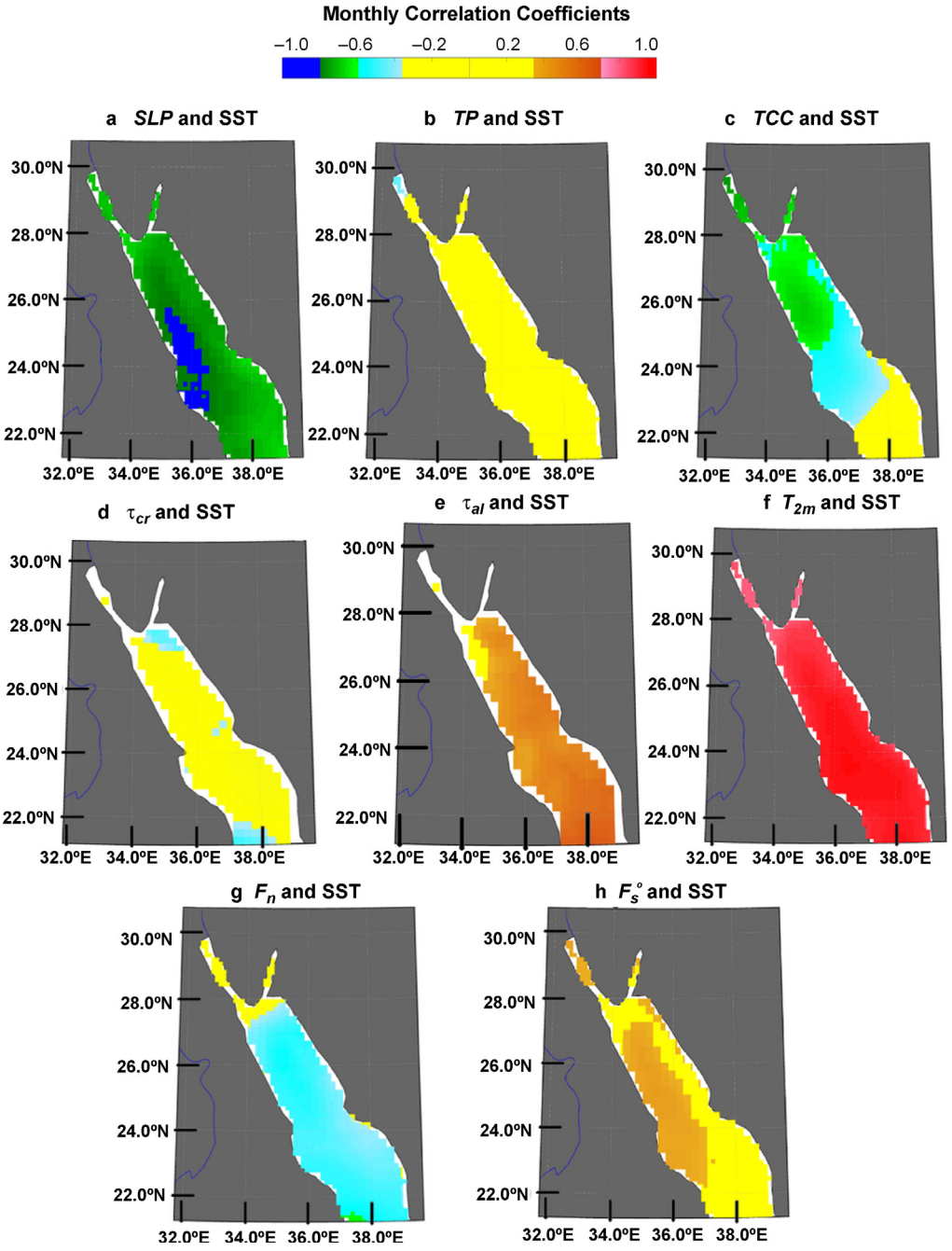

Figure 10 Monthly correlation coefficients between the SST and the studied atmospheric components.

approximately 7% (July)–16% (March) of the NRS, most significantly over the central and northeastern portions of the study area, which indicates higher Chl-*a* values. Permanent downwelling events comprised approximately 10% (September)–26% (February) of the NRS, most significantly over the northwestern portion of the study area.

3.6. Chlorophyll-*a*

Generally, a sharp increase in Chl-*a* values occurred in the southern region of the Red Sea compared to the northern region (Acker et al., 2008). The NRS is characterized by a few patches of high Chl-*a* values that are surrounded by a large area of relatively lower Chl-*a* values (Acker et al., 2008). The Chl-*a* shows a seasonal variation over the Gulf of Aqaba, while the upper waters are much more productive (Chl-*a* from 33 to 70 mg m^{-3}) during winter (Levanon-Spanier et al., 1979; Stambler, 2005). MODIS_L3_Chl-*a* showed distinct seasonal variation over the NRS, reaching its maximum value during cold months (more than 0.49 $\mu g\ L^{-1}$), especially along the eastern coasts (Fig. 16). This result can be explained by the high frequency of upwelling events during the cold season along the eastern coasts. In addition, MODIS_L3_Chl-*a* showed distinct meridional variation from November to January, which was partly associated with the current findings of the meridional SST fronts and supports the previous findings

Table 1 Percentage of the study area that was significantly correlated with the studied atmospheric components; the monthly correlation coefficients between the SST and the studied atmospheric components were computed over the study area (n = 180, level of significance = 95%).

	Annual [%]			
	Winter [%]	Spring [%]	Summer [%]	Autumn [%]
Sea level pressure (*SLP*)	100			
	4	100	37	100
Total precipitation (*TP*)	2			
	31	5	11	2
Total cloud cover (T_{CC})	75			
	6	99	0	56
Cross-shore wind stress (τ_{cr})	12			
	94	2	56	35
Alongshore wind stress (τ_{al})	88			
	82	24	44	81
Air temperature 2 m above sea level (T_{2m})	100			
	71	100	95	100
Net heat loss from the sea (F_n)	95			
	2	8	1	100
Solar radiation to the open water surface (F_s^o)	43			
	19	100	16	100

Table 2 PCA Statistics and component matrix of various atmospheric parameters (n = 5479).

Principal component analysis									
	PC(1)	PC(2)	PC(3)	PC(4)	PC(5)	PC(6)	PC(7)	PC(8)	PC(9)
Variance	3.60	1.67	1.21	0.82	0.78	0.49	0.27	0.12	0.02
Proportion	0.40	0.19	0.13	0.09	0.09	0.05	0.03	0.01	0.00
Cum. proportion	40.0%	58.6%	72.1%	81.3%	90.0%	95.4%	98.4%	99.7%	100.0%
Loadings	PC(1)	PC(2)	PC(3)	PC(4)	PC(5)	PC(6)	PC(7)	PC(8)	PC(9)
SST	**0.415**	0.117	−0.225	0.543	−0.053	−0.006	0.367	0.245	0.520
T_{2m}	**0.502**	0.071	−0.067	0.206	−0.036	−0.198	−0.037	0.264	−0.764
SLP	**−0.489**	−0.091	0.101	0.102	0.023	0.207	0.071	0.822	−0.085
T_{CC}	−0.212	0.495	0.048	−0.227	**−0.529**	**−0.540**	0.281	0.080	0.021
TP	−0.112	0.430	−0.306	−0.140	**0.784**	−0.256	0.057	0.075	0.008
τ_{al}	0.213	0.060	**−0.594**	**−0.568**	−0.214	0.442	0.096	0.162	−0.008
τ_{cr}	0.185	0.405	**0.583**	−0.127	0.141	0.475	0.430	−0.073	−0.102
F_n	**0.418**	0.080	0.359	−0.338	0.041	−0.162	−0.528	0.377	0.355
F_s^o	−0.159	**0.607**	−0.133	0.357	−0.185	0.337	−0.551	−0.090	−0.023

of Tong et al. (2010). Moreover, MODIS_L3_Chl-*a* reached its lowest values (less than 0.14 μg L^{-1}) over the Gulf of Aqaba, most markedly during hot months.

The monthly correlations between MODIS_L3_Chl-*a* and the studied parameters, including the SST, τ_{cr} and τ_{al}, were significant over 87%, 62% and 34% of the study area, respectively (Fig. 17), with distinct seasonal variation. SST was significantly negatively correlated with MODIS_L3_Chl-*a* over 41%, 41%, 14%, and 95% of the study area during winter, spring, summer, and autumn, respectively (most markedly between 24 and 28°N). Moreover, τ_{cr} had no significant correlation with MODIS_L3_Chl-*a* over 13%, 2%, 16%, and 16% of the study area during winter, spring, summer, and autumn, respectively. However, τ_{al} was inversely correlated with MODIS_L3_Chl-*a* over 6%, 13%, 19%, and 80% of the study area during winter, spring, summer, and autumn, respectively (most noticeably over the northeastern corner of the NRS).

Generally, the SST influence on MODIS_L3_Chl-*a* was significant after removing the effect of the annual cycle (Fig. 17b). The monthly correlation between the SST and MODIS_L3_Chl-*a* after removing the annual cycle effect was significant over 71% of the study area (approximately 12% less compared to before removing the annual cycle). This result indicates that the correlation coefficient between the SST and MODIS_L3_Chl-*a* had no significant dependence on a seasonal cycle.

In addition, PCA was run between the Chl-*a* and the SST, τ_{cr} and τ_{al}. The analysis showed that 94% of the overall variance was explained by the first three principal components and 84% by only the first two principal components. The first

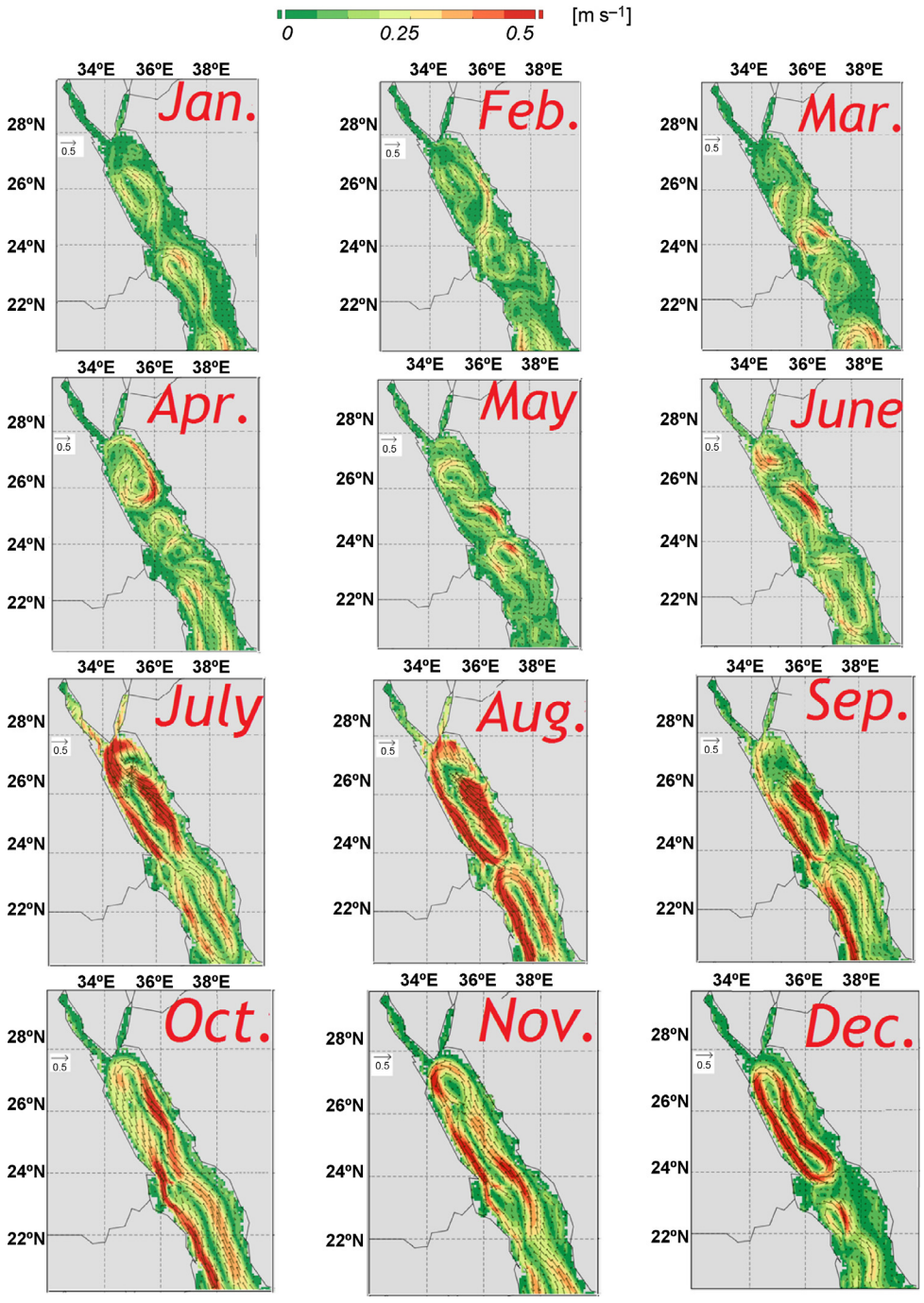

Figure 11 HYCOM's monthly averaged surface currents during 2010–2014.

component (PC1, 56.1% of the overall variance) was dominated by the SST and τ_{al}. The second component (PC2, 28% of the overall variance) was dominated by τ_{cr}. The third component (PC3, 9% of the overall variance) was related to the τ_{al}.

4. Discussion

This study combined long-term remote sensing data and reanalyzed data with a global circulation model (HYCOM) to understand the interactions between the sea surface temperature, surface wind and oceanic dynamics in the NRS, including the surface circulation, mixed layer depth, upwelling, and Chl-*a*.

The accuracy of the various databases was examined and validated. The accuracy of scatterometer ASCAT/QUICK SCAT data is sufficient to study local oceanic SW features over open sea regions (Ebuchi et al., 2002; Li et al., 2012; Pickett et al., 2003). Scatterometer ASCAT/QUICK SCAT has a coarse resolution (Chang et al., 2015), which may heighten the level of uncertainty in coastal areas. Thus, the scatterometer data

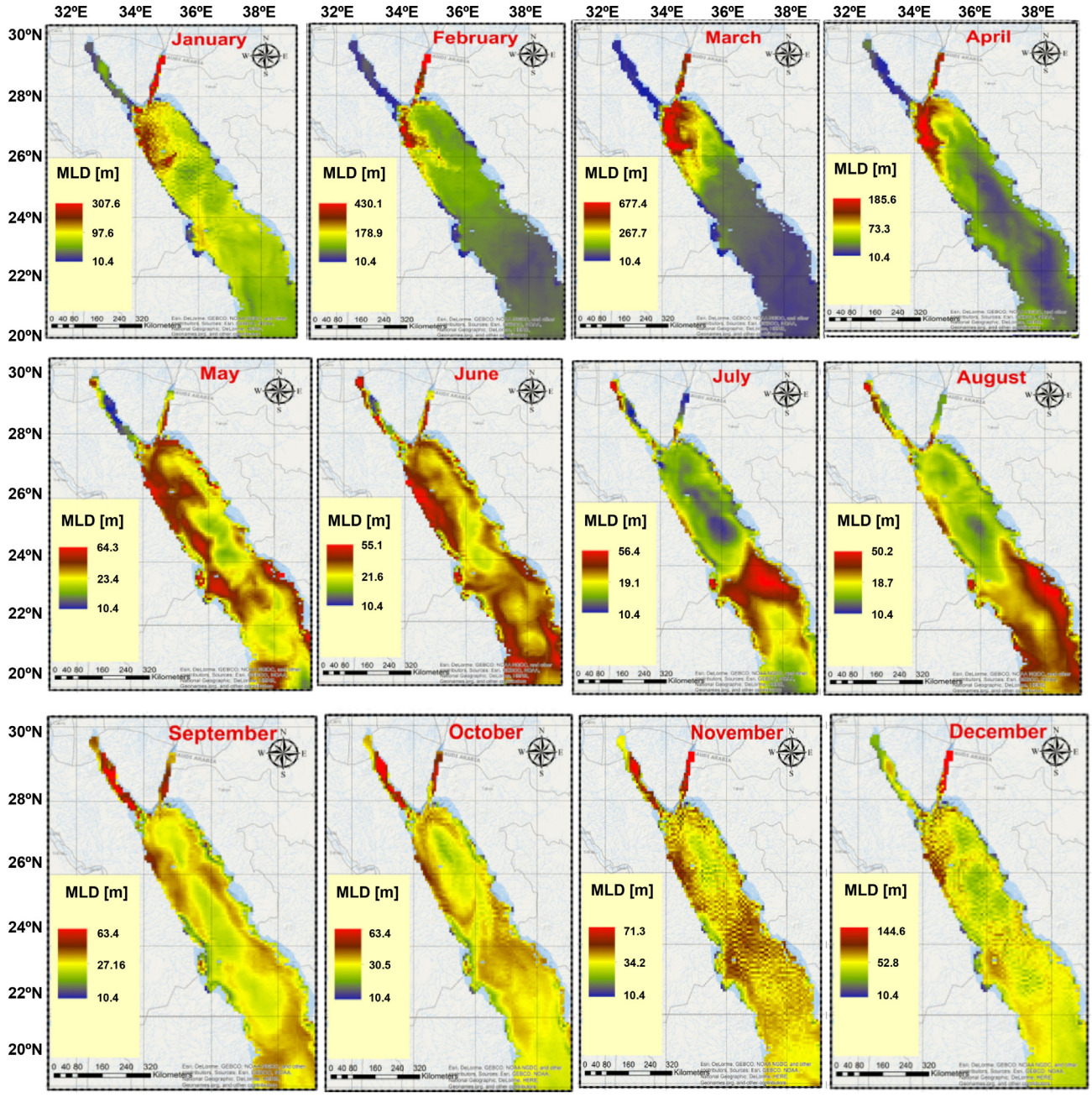

Figure 12 Monthly distributions of the HYCOM's mixed layer depth (2010–2014).

were used to study the local features of the open NRS regions alongside the general features of the coastal area. The AVHRR's SST data were constructed by combining observations from different platforms (satellites, ships, and buoys) on a regular global grid and are considered an effective tool to study oceanic SST (Reynolds et al., 2007). The accuracy of the AVHRR's SST (version 2) increases by using the ship bias correction (Reynolds et al., 2007). The AVHRR's SST resolution is sufficient to study local oceanic features (Marullo et al., 2007; Nykjaer et al., 2009; Shaltout and Omstedt, 2014). ECMWF Era Interim data ($0.75^\circ \times 0.75^\circ$) generally match observations (Berrisford et al., 2009; Shaltout et al., 2013). The sensitivity of the $1/12^\circ$ HYCOM daily output over the Red Sea was further analyzed by running two validation experiments (one for SST and a second for MLD) with remotely sensed and observed data. The various databases provided relevant tools to study oceanic parameters, including the SW, SST, MLD, and Chl-*a*, and the atmospheric parameters T_{2m}, *SLP*, *P*, *TCC*, and air–sea heat fluxes.

The NRS surface wind speed magnitude was 6 m s^{-1} on average, with a dominant northwesterly direction, and no significant trend was identified over the years of 2000–2014. This weaker wind speed can be explained by the smooth sea level pressure over the NRS. The NRS surface temperature was 5°C warmer than that of the adjacent basin of the Mediterranean Sea (Levantine sub-basin), and the warming trend was approximately 70% higher than that of the Levantine sub-basin (Shaltout and Omstedt, 2014). In addition, the

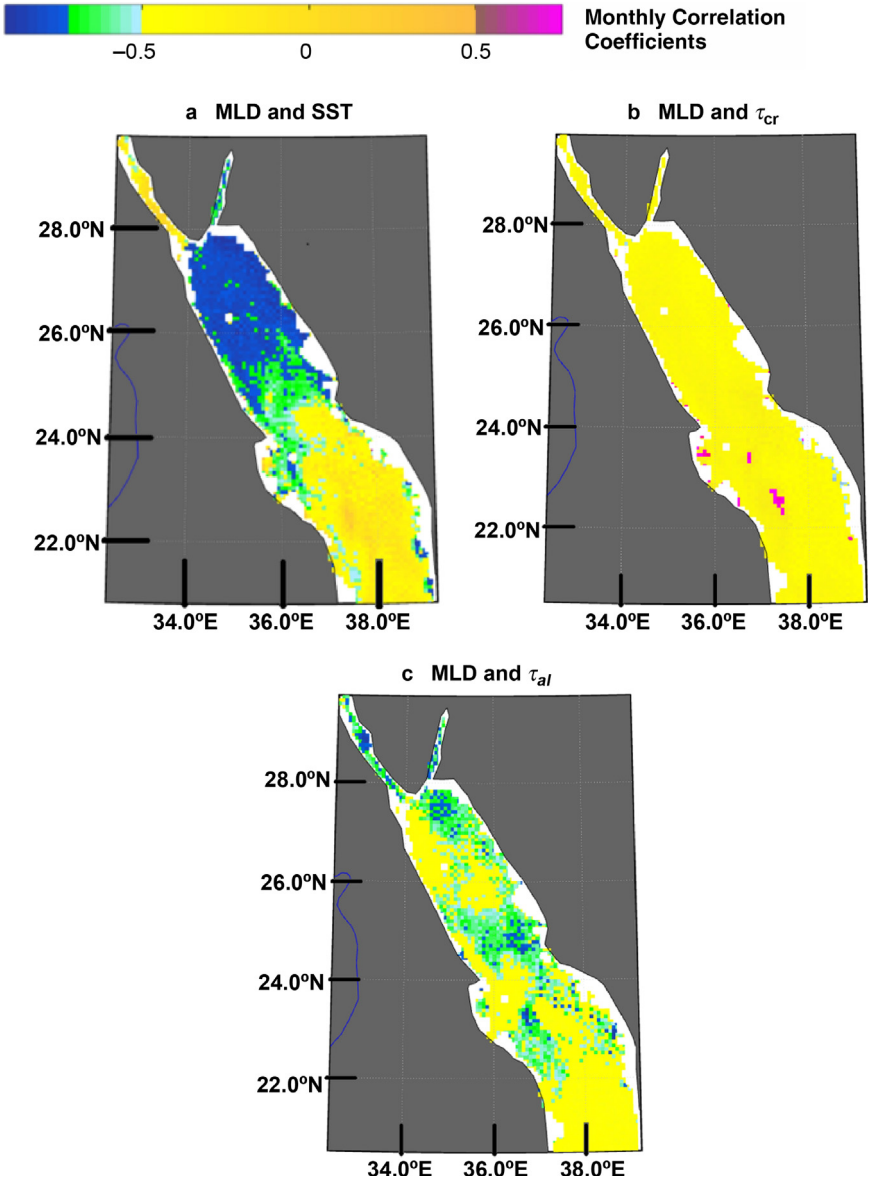

Figure 13 Monthly correlation coefficients between the MLD and various studied parameters (SST, τ_{cr}, and τ_{al}).

seasonality amplitude of the NRS surface temperature was less than 1/3 that of the Levantine sub-basin, which indicates that the Levantine sub-basin is more dynamic (Shaltout and Omstedt, 2014). The SST over the NRS had an annual average of 26°C, with a seasonality amplitude of 3°C and an insignificant trend over the years of 2000–2014.

The surface circulation over the NRS revealed significant monthly variations and was characterized by eastern boundary currents (moving toward the north, especially during cold months), western boundary currents (moving toward the south, especially during cold months), and cross-basin currents (particularly during hot months). The sea surface temperature spatial distribution closely matched the currents distribution, while the surface wind supported the current system only along the western coasts. The Gulf of Suez and Gulf of Aqaba were not significantly affected by the Red Sea surface circulation. The current result supports previous findings of Yao et al. (2014) based on the simulations performed with the Mitgcm model. The circulation pattern in the NRS depends on the buoyancy loss from evaporation. The density to the greatly increased to the north during summer (July, August, and September), which was associated with the highest evaporation rate, and the highest northward pressure gradient existed with the sea surface slope. This phenomenon enhanced the generation of an eastward cross-basin geostrophic current in the surface layer and increased the probability of a shift from one cyclonic gyre to two gyre systems during summer.

The NRS mixed layer depth showed distinct monthly variation, and the current results support the previous findings of Genin et al. (1995) and Labiosa et al. (2003). The NRS mixed layer depth showed an annual average of 29 m, mostly over the Gulf of Aqaba and the northwestern coast of the NRS. The NRS mixed layer depth generally followed the sea surface temperature only over the sea's northern section. MLD was highly connected to the

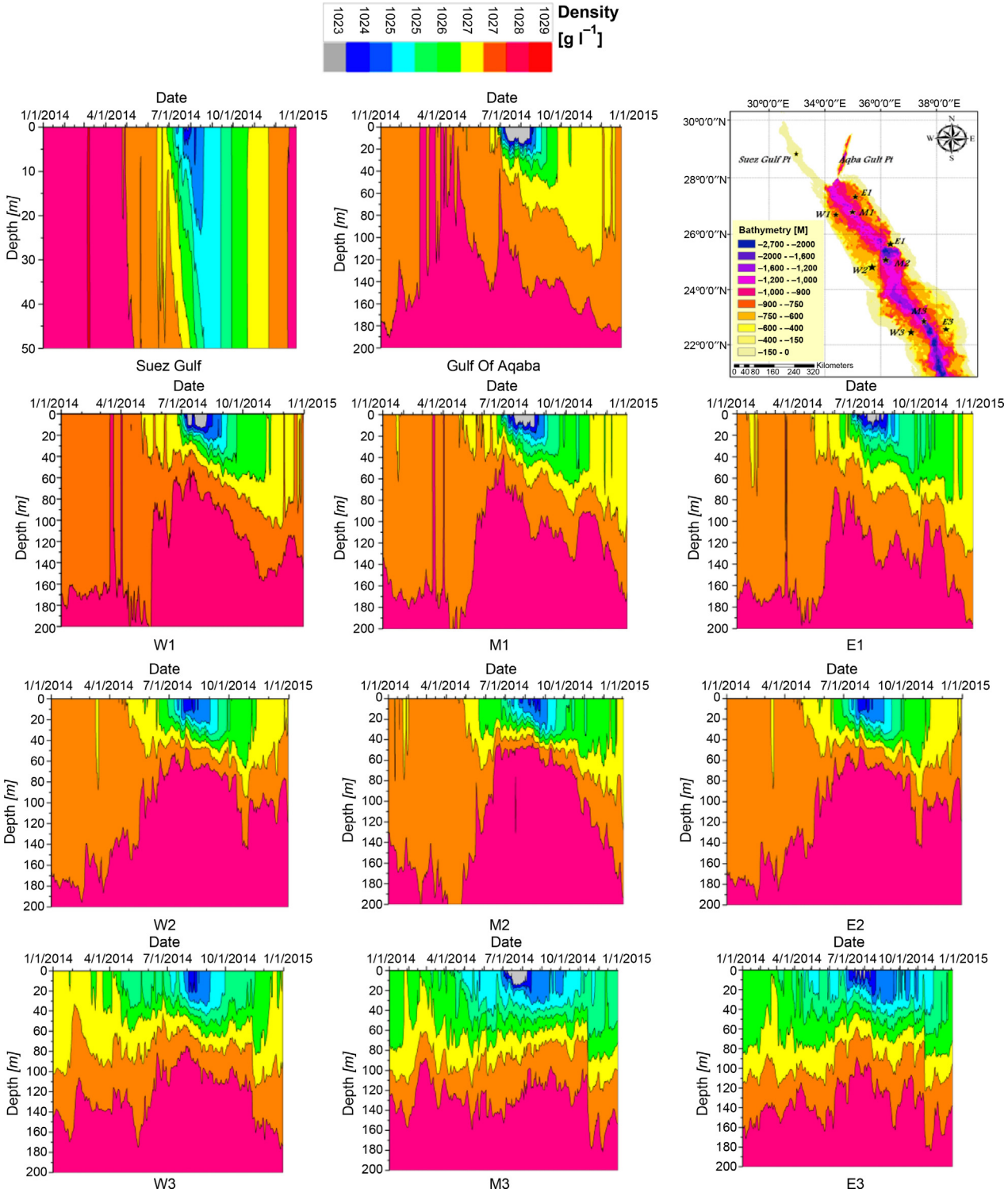

Figure 14 Density profiles at specific locations based on daily HYCOM results (2014).

circulation patterns over the NRS. For example, the sudden drop in the MLD values at 24°N in July and August can be directly linked to the two dominant anticyclonic gyres that were previously discussed.

Intermediate layer vertical velocities were calculated from the HYCOM results, which showed permanent upwelling (downwelling) events over 13% (18%) of the study area. The surface wind stress and surface stratification significantly affected the vertical surface velocity. Yao et al. (2014) studied upwelling and downwelling mechanisms by using a higher resolution model over the NRS. Their study suggested that the cold western boundary layer was associated with upwelling and the warm eastern boundary current was associated with downwelling. In addition, the western upwelling

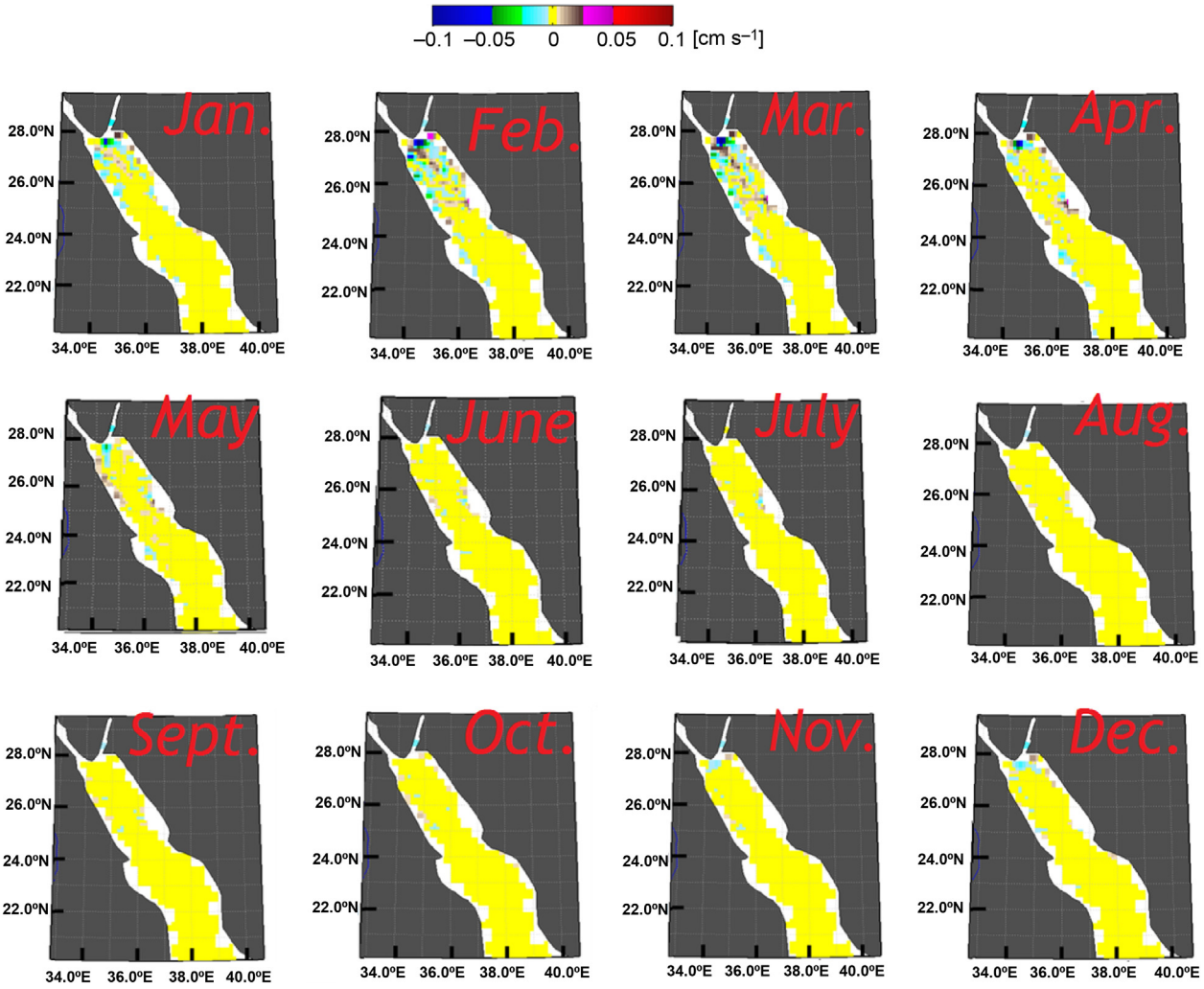

Figure 15 Monthly distributions of the HYCOM's vertical velocities for the intermediate layer (2010–2014).

velocity was markedly weaker than the average downwelling velocity in the eastern boundary through the upper 300 m.

Generally, MODIS_L3_Chl-*a* over the Gulf of Aqaba was lower than that in the Gulf of Suez, partly because of the shallower water depth in the Gulf of Suez compared to the Gulf of Aqaba (the average depth of the Gulf of Aqaba is more than 11 times that of the Gulf of Suez). Labiosa et al. (2003) studied the spatial patterns of phytoplankton Chl-*a* in the Gulf of Aqaba, which is a warm and nutrient-poor region. Unlike other oligotrophic regions (e.g. the Mediterranean Sea or oligotrophic North Pacific), the Gulf of Aqaba's weak stratification and upwelling-favorable wind facilitate the existence of phytoplankton.

Chl-*a* was highly correlated with the sea surface temperature (including or excluding the seasonal cycle), and the maximum Chl-*a* was found over the Gulf of Suez and along the eastern coast. The seasonal cycles of the Chl-*a* and sea surface temperature were only responsible for 10% of their correlation, which supports the previous findings of Raitsos et al. (2013) but contrasts Koblentz-Mishke et al. (1970) results. This disagreement may be explained by the better precision of the data that were used in the current study. The wind stress had a smaller effect on the Chl-*a* compared to the sea surface temperature, but the relatively high correlation between MODIS_L3_Chl-*a* and τ_{al} over the eastern basin can be explained by the alongshore component, which was always higher than the cross-shore component. In addition, the continuously high values of the alongshore (northwesterly direction) winds enhanced the formation of the cyclonic gyre (eastern current moving to the north), which brought nutrient-rich waters from the southern Red Sea. The annual average Chl-*a* value over the NRS was approximately 0.23 $\mu g\ L^{-1}$, most significantly during cold seasons. Generally, the NRS had a low Chl-*a* of 0.23 $\mu g\ L^{-1}$ on average (Chl-*a* $< 0.25\ \mu g\ L^{-1}$ over 78% of the global ocean area; Hu et al., 2012), which is characteristic of oligotrophic waters ($<0.8\ \mu g\ L^{-1}$; Gons et al., 2008; Gregg and Rousseaux, 2014).

Cyclonic gyres were the main drivers of the SST in the northern portion of the NRS, which intensified the eastern area's SST or moderated the surface cooling in the northernmost and western-most areas. The stronger the cyclonic gyre, the more meridional the SST distribution became. In addition, continuous gyre circulation in the northern area enhanced the upwelling process. These continuous gyres affected the surface layer Chl-*a* by feeding the northern area with nutrients. Gyre-related upwelling is an occasional provider of nutrients to the surface layers from nutrient-rich deep layers (Williams and Follows, 2011). Additional

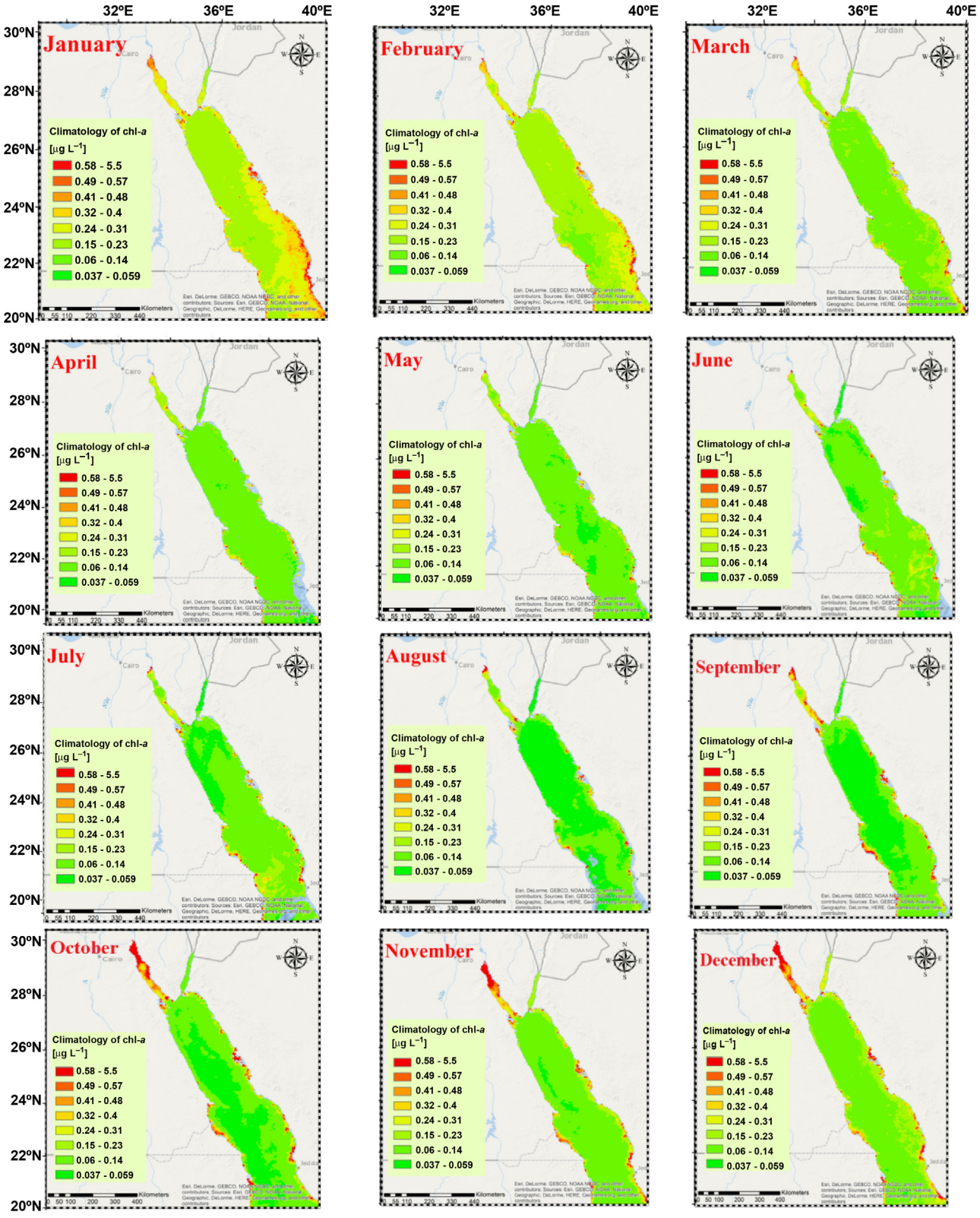

Figure 16 Chl-*a* climatology based on the last five years of MODIS AQUA data (2010–2014).

evidence for this mechanism was provided by Raitsos et al. (2013): the winter of 2012 was associated with exceptionally high Chl-*a*. On the contrary, the weak activity of the gyres and weak atmospheric forcing during the second half of 2009 (prior to the warm 2010 winter) resulted in the warmest winter SST during this 12-year period. In addition, the low gyre activity suspended the nutrient supply from deeper layers, which is reflected in the lowest Chl-*a* in the winter of 2010. Reef-bound coastal waters, especially in the south-eastern area of the NRS, had relatively higher

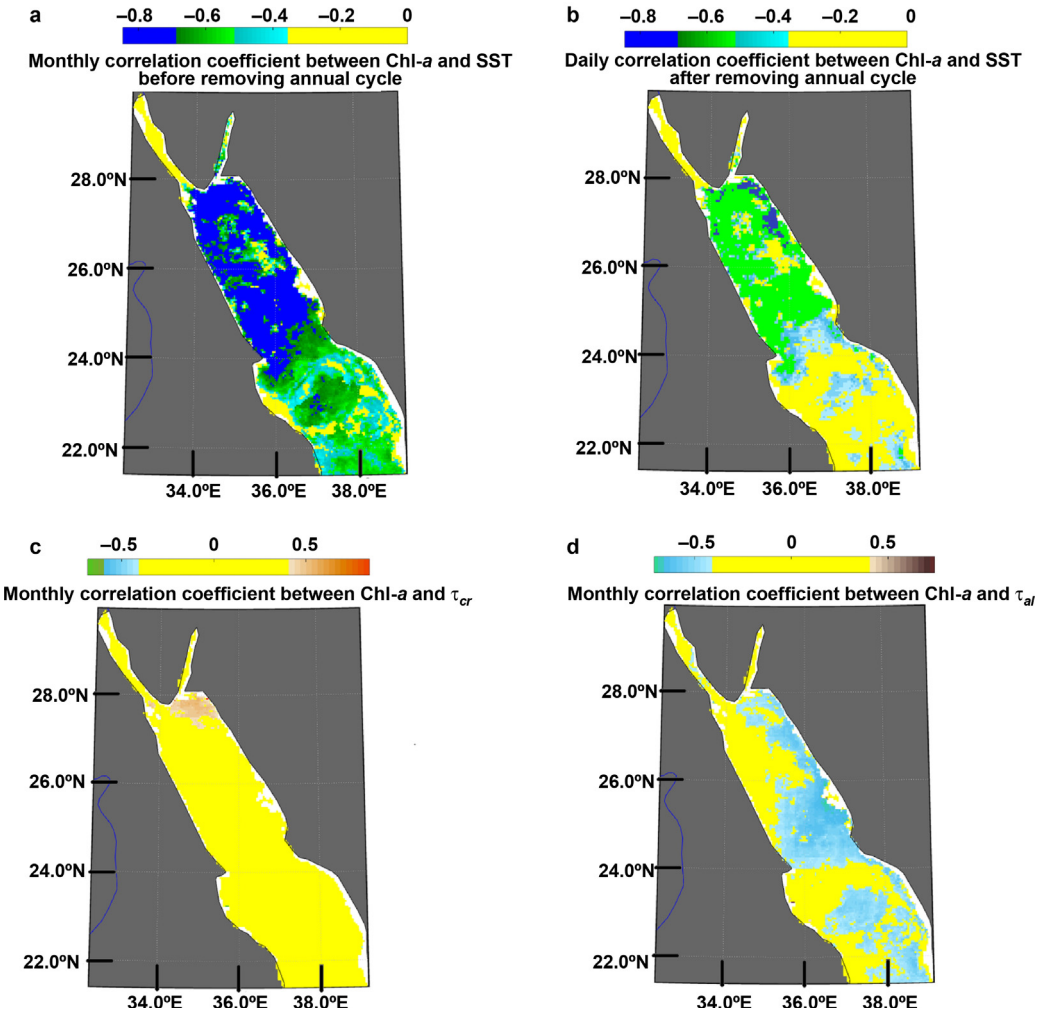

Figure 17 Monthly correlation coefficients between Chl-*a* and various studied parameter (SST, τ_{al}, and τ_{cr}; the annual cycle was not removed for the surface wind stress because of the weak wind stress annual cycle).

Chl-*a*. Moreover, the nutrient concentrations in these reef-bound coastal waters significantly exceeded those in the offshore waters. This difference may be as a result of nutrient release from regenerative spaces in the reef framework and coral sand. The most nutrient-poor waters are located in the NRS, while the southern Red Sea receives some nutrients from intermediate water inflow through the Gulf of Aden during the summer (Acker et al., 2008). Another possible direct effect of the eastern boundary current (moving to the north) is the feeding of the eastern area of the NRS with relatively nutrient-rich water masses from the southern Red Sea.

5. Conclusions

SW speed data trend analysis with normal linear regression indicated a significantly decreasing trend of 0.2 m s^{-1} decade^{-1} that was associated with a significant SST warming trend of 0.3°C decade^{-1} and no significant Chl-*a* trend during 2000–2014. The STL method showed that the trend was not significant and constant seasonality in the SW speed. In addition, STL confirmed slight increasing trends in the SST during the study period (2010–2015). The STL method proved to be a more realistic procedure to assess trends in the SW speed and SST. The NRS had an average annual SW of 6 m s^{-1}, SST of 26°C, MLD of 29 m and Chl-*a* of 0.236 μg L^{-1}, along with low active vertical velocity.

This study confirmed the applicability of satellite remote sensing as a powerful tool to detect SST fronts. Applying a single Cayula–Cornillon algorithm proved that fronts were more frequent in December, January, and February. The Egypt-Saudi Arabia Fronts (ESAF) became significant in December and January. As the formation of the eastern and western boundary currents advanced, the occurrence of meridional fronts was also enhanced. Sharp horizontal contrasts in the Chl-*a* values, especially in January, can be directly linked to the existence of these strong meridional fronts. Moreover, the HYCOM results provided a realistic tool to study the NRS general circulation patterns and identify the seasonal MLD dynamics.

This study highlighted the influences of atmospheric parameters such as T_{2m}, τ_{cr}, τ_{al}, F_n, F_s^o, *TCC*, *SLP*, and *TP* on the SST and suggests that the effects of T_{2m}, *SLP* and F_n were dominant and can explain 94.6% of the general SST variations over the NRS. Moreover, the PCA results indicated that 81.3% of the overall variance was explained by the first four principal components. The main controlling factor for the spatial

variation of Chl-*a* is the relatively higher MLD in the northwestern part resulting in an enhancement of convective overturning. In addition, the alongshore (northwesterly direction) winds enhanced the formation of the cyclonic gyre, which brought nutrient-rich waters from the southern Red Sea resulting in higher Chl-*a* in the western coastal region. The current study indicated that the effects of the SST and τ_{al} on Chl-*a* and MLD were predominant. Moreover, removing the annual SST cycle only slightly decreased the effect of the SST on Chl-*a* by approximately 10%, which indicates that the SST directly affects the Chl-*a*. The alongshore wind component had a dominant effect on SST, MLD, and Chl-*a* in the cross-shore component.

The surface circulation over the NRS was characterized by warmer eastern boundary currents (moving to the north) and western boundary currents (moving to the south). The eastern boundary current turned southward and fed the western boundary current, forming the NRS's cyclonic circulation. The circulation patterns and the atmospheric forcing can explain the spatial distribution of SST in the NRS. The monthly spatial distribution of the upwelling showed that it is dominant in the northeastern area of the Red Sea. However, the warming effect of the eastern boundary current on SST in the northeastern area appeared to predominate over the cooling effect from this upwelling. Indeed, the results from the HYCOM global circulation model provided insight into the possible mechanisms through which the considered parameters interacted with the dominant circulation and vertical stratification patterns. Generally, the data that were used in this study, including remotely sensed data and oceanic models, served as realistic tools to study the local features of the open NRS; however, coastal and shallow areas require more attention. The use of a more accurate regional oceanic model with higher resolution could provide a realistic evaluation of coastal shallow areas.

More holistic and multidisciplinary research is required to more accurately identify the mechanisms that are related to the SST, Chl-*a*, and upwelling. The results of this study may be utilized to inform future work to examine the potential effects of the water temperature and surface winds on mass coral bleaching, and air–sea CO_2 flux.

Acknowledgments

The first author was supported by a scholarship from the Mission Department, Ministry of Higher Education of the Government of Egypt, which is gratefully acknowledged. This research was undertaken when Ahmed Eladawy was a visiting junior researcher at Nadaoka-lab (Tokyo Institute of Technology). The Hurghada Environmental Protection and Conservation Association (HEPCA) is also acknowledged for providing the measured water temperature data. Lawrence Patrick Bernardo (Tokyo Institute of Technology) and Prof. Vassilis P. Papadopoulos (Hellenic Centre for Marine Research) are acknowledged for their efforts toward revising the manuscript. We are grateful to the National Climatic Data Center (NCDC) and National Oceanic and Atmospheric Administration (NOAA) for providing the remotely sensed datasets through their websites. In addition, the authors are grateful to Tokyo Institute of Technology, and the Japan International Cooperation Agency (JICA).

References

Abdi, H., Williams, L.J., 2010. Principal component analysis. WIREs Comput. Stat. 2 (4), 433–459, http://dx.doi.org/10.1002/wics.101.

Abualnaja, Y., Papadopoulos, V.P., Josey, S.A., Hoteit, I., Kontoyiannis, H., Raitsos, D.E., 2015. Impacts of climate modes on air–sea heat exchange in the Red Sea. J. Clim. 28 (7), 2665–2681, http://dx.doi.org/10.1175/JCLI-D-14-00379.1.

Acker, J., Leptoukh, G., Shen, S., Zhu, T., Kempler, S., 2008. Remotely-sensed chlorophyll *a* observations of the northern Red Sea indicate seasonal variability and influence of coastal reefs. J. Mar. Syst. 69 (3), 191–204, http://dx.doi.org/10.1016/j.jmarsys.2005.12.006.

Al-Horani, F.A., Al-Rousan, S.A., Al-Zibdeh, M., Khalaf, M.A., 2006. The status of coral reefs on the Jordanian coast of the Gulf of Aqaba, Red Sea. Zool. Middle East 38 (1), 99–110, http://dx.doi.org/10.1080/09397140.2006.10638171.

Al-Rousan, S., Al-Taani, A.A., Rashdan, M., 2016. Effects of pollution on the geochemical properties of marine sediments across the fringing reef of Aqaba, Red Sea. Mar. Pollut. Bull. 110 (1), 546–554, http://dx.doi.org/10.1016/j.marpolbul.2016.05.038.

Barale, V., Gade, M., 2013. Remote Sensing of the African Seas. Springer, 317–337, http://dx.doi.org/10.1007/978-94-017-8008-7.

Belkin, I., Cornillon, P., 2003. SST fronts of the Pacific coastal and marginal seas. Pac. Oceanogr. 1 (2), 90–113.

Belkin, I.M., Cornillon, P.C., 2007. Fronts in the world ocean's large marine ecosystems. ICES C 500 (130) 21 pp.

Belkin, I.M., Cornillon, P., Ullman, D., 2003. Ocean fronts around Alaska from satellite SST data. In: Proceedings of the American Meteorological Society's 7th Conference on the Polar Meteorology and Oceanography and Joint Symposium on High-Latitude Climate Variations. 12–16 May, Hyannis, MA, Paper no 12.7 15 pp.

Bentamy, Abderrahim, Croize-Fillon, Denis, 2012. Gridded surface wind fields from Metop/ASCAT measurements. Int. J. Remote Sens. 33 (6), 1729–1754, http://dx.doi.org/10.1080/01431161.2011.600348.

Berman, T., Paldor, N., Brenner, S., 2003. Annual SST cycle in the Eastern Mediterranean, Red Sea and Gulf of Elat. Geophys. Res. Lett. 30 (5), 1261, 4 pp., http://dx.doi.org/10.1029/2002GL015860.

Berrisford, P., Dee, D., Fielding, K., Fuentes, M., Kallberg, P., Kobayashi, S., Uppala, S., 2009. The ERA-Interim Archive, ERA Report Series. European Centre for Medium Range Weather Forecasts Shinfield Park, UK, 20 pp.

Bleck, R., 2002. An oceanic general circulation model framed in hybrid isopycnic-Cartesian coordinates. Ocean Model. 4 (1), 55–88, http://dx.doi.org/10.1016/S1463-5003(01)00012-9.

Blythe, J.N., Silva, C.B., Pineda, J., 2011. Nearshore, seasonally persistent fronts in sea surface temperature on Red Sea tropical reefs. ICES J. Mar. Sci. 68, 1827–1832, http://dx.doi.org/10.1093/icesjms/fsr109.

Bower, A.S., Farrar, J.T., 2015. Air–sea interaction and horizontal circulation in the Red Sea. In: The Red Sea. Springer Earth System Sciences. Springer-Verlag, Berlin/Heidelberg, 329–342, http://dx.doi.org/10.1007/978-3-662-45201-1_19.

Boyer, J.N., Kelble, C.R., Ortner, P.B., Rudnick, D.T., 2009. Phytoplankton bloom status: chlorophyll *a* biomass as an indicator of water quality condition in the southern estuaries of Florida, USA. Ecol. Indic. 9 (6), S56–S67, http://dx.doi.org/10.1016/j.ecolind.2008.11.013.

Boyer, T.P., Antonov, J.I., Baranova, O.K., Coleman, C., Garcia, H.E., Grodsky, A., Johnson, D.R., Locarnini, R.A., Mishonov, A.V., O'Brien, T.D., Paver, C.R., Reagan, J.R., Seidov, D., Smolyar, I. V., Zweng, M.M., 2013. World Ocean Database 2013, NOAA Atlas NESDIS 72. National Oceanographic Data Center, Ocean Climate

Laboratory, Silver Spring, MD, 209 pp., http://dx.doi.org/10.7289/V5NZ85MT.

Brewin, R.J.W., Raitsos, D.E., Pradhan, Y., Hoteit, I., 2013. Comparison of chlorophyll in the Red Sea derived from MODIS-Aqua and in vivo fluorescence. Remote Sens. Environ. 136, 218—224, http://dx.doi.org/10.1016/j.rse.2013.04.018.

Carder, K.L., Chen, F.R., Cannizzaro, J.P., Campbell, J.W., Mitchell, B.G., 2004. Performance of the MODIS semi-analytical ocean color algorithm for chlorophyll-*a*. Adv. Sp. Res. 33 (7), 1152—1159, http://dx.doi.org/10.1016/S0273-1177(03)00365-X.

Carlson, D.F., Fredj, E., Gildor, H., 2014. The annual cycle of vertical mixing and restratification in the Northern Gulf of Eilat/Aqaba (Red Sea) based on high temporal and vertical resolution observations. Deep-Sea Res. Pt. I 84, 1—17, http://dx.doi.org/10.1016/j.dsr.2013.10.004.

Casey, K.S., Brandon, T.B., Cornillon, P., Evans, R., 2010. The Past, Present, and Future of the AVHRR Pathfinder SST Program [in:] Oceanography from Space. Springer, Netherlands, 273—287, http://dx.doi.org/10.1007/978-90-481-8681-5_16.

Cayula, J.-F., Cornillon, P., 1992. Edge detection algorithm for SST images. J. Atmos. Ocean. Technol. 9 (1), 67—80, http://dx.doi.org/10.1175/1520-0426(1992)009<0067:EDAFSI>2.0.CO;2.

Chang, R., Rong, Z., Badger, M., Hasager, C.B., Xing, X., Jiang, Y., 2015. Offshore wind resources assessment from multiple satellite data and WRF modeling over South China Sea. Remote Sens. 7 (1), 467—487, http://dx.doi.org/10.3390/rs70100467.

Chu, P.C., 1989. Relationship between thermally forced surface wind and sea surface temperature gradient. Pure Appl. Geophys. 130 (1), 31—45, http://dx.doi.org/10.1007/BF00877735.

Clerici, M., Melin, F., Hoepffner, N., 2008. MERSEA-IP Marine EnviRonment and Security for the European Area; Assessment of Global Ocean Colour Products against In-situ Datasets. European Commission, Ispra, 44 pp.

Cleveland, R.B., Cleveland, W.S., McRae, J.E., Terpenning, I., 1990. STL: a seasonal-trend decomposition procedure based on loess. J. Off. Stat. 6 (1), 3—73.

Curran, P.J., Dungan, J.L., Gholz, H.L., 1990. Exploring the relationship between reflectance red edge and chlorophyll content in slash pine. Tree Physiol. 7 (1—4), 33—48, http://dx.doi.org/10.1093/treephys/7.1-2-3-4.33.

De Boyer Montégut, C., Madec, G., Fischer, A.S., Lazar, A., Iudicone, D., 2004. Mixed layer depth over the global ocean: an examination of profile data and a profile-based climatology. J. Geophys. Res.-Oceans 109 (C12), 20 pp., http://dx.doi.org/10.1029/2004jc002378.

Dee, D.P., Uppala, S.M., Simmons, A.J., Berrisford, P., Poli, P., Kobayashi, S., Andrae, U., Balmaseda, M.A., Balsamo, G., Bauer, P., Bechtold, P., Beljaars, A.C.M., van de Berg, L., Bidlot, J., Bormann, N., Delsol, C., Dragani, R., Fuentes, M., Geer, A.J., Haimberger, L., Healy, S.B., Hersbach, H., Hólm, E.V., Isaksen, L., Kållberg, P., Köhler, M., Matricardi, M., Mcnally, A.P., Monge-Sanz, B.M., Morcrette, J.J., Park, B.K., Peubey, C., de Rosnay, P., Tavolato, C., Thépaut, J.N., Vitart, F., 2011. The ERA-Interim reanalysis: configuration and performance of the data assimilation system. Q. J. R. Meteorol. Soc. 137 (656), 553—597, http://dx.doi.org/10.1002/qj.828.

Ebuchi, N., Graber, H.C., Caruso, M.J., 2002. Evaluation of wind vectors observed by QuikSCAT/SeaWinds using ocean buoy data. J. Atmos. Ocean. Technol. 19 (12), 2049—2062, http://dx.doi.org/10.1175/1520-0426(2002)019<2049:EOWVOB>2.0.CO;2.

Falkowski, P.G., Barber, R.T., Smetacek, V., 1998. Biogeochemical controls and feedbacks on ocean primary production. Science 281 (5374), 200—206.

Furby, K.A., Bouwmeester, J., Berumen, M.L., 2013. Susceptibility of central Red Sea corals during a major bleaching event. Coral Reefs 32 (2), 505—513, http://dx.doi.org/10.1007/s00338-012-0998-5.

Gai, S., Wang, H., Liu, G., Huang, L., Song, X., 2012. Chlorophyll *a* increase induced by surface winds in the northern South China Sea. Acta Oceanol. Sin. 31 (4), 76—88, http://dx.doi.org/10.1007/s13131-012-0222-z.

Genin, A., Lazar, B., Brenner, S., 1995. Vertical mixing and coral death in the Red Sea following the eruption of Mount Pinatubo 1995. Nature 377 (6549), 507—510.

Giannini, A., Kushnir, Y., Cane, M.A., 2000. Interannual variability of Caribbean rainfall, ENSO, and the Atlantic Ocean. J. Clim. 13 (2), 297—311.

Gons, H.J., Auer, M.T., Effler, S.W., 2008. MERIS satellite chlorophyll mapping of oligotrophic and eutrophic waters in the Laurentian Great Lakes. Remote Sens. Environ. 112 (11), 4098—4106, http://dx.doi.org/10.1016/j.rse.2007.06.029.

Gregg, W.W., Rousseaux, C.S., 2014. Decadal trends in global pelagic ocean chlorophyll: a new assessment integrating multiple satellites, in situ data, and models. J. Geophys. Res. Oceans 119 (9), 5921—5933, http://dx.doi.org/10.1002/2014JC010158.

Halliwell, G., 2004a. Diagnosis of Kinematic Vertical Velocity in HYCOM, Tech Report, 7 pp.

Halliwell, G.R., 2004b. Evaluation of vertical coordinate and vertical mixing algorithms in the HYbrid-Coordinate Ocean Model (HYCOM). Ocean Model. 7 (3), 285—322, http://dx.doi.org/10.1016/j.ocemod.2003.10.002.

Heileman, S., Mistafa, N., 2008. III-6 Red Sea: LME# 33, The UNEP Large Marine Ecosystem Report: A Perspective on Changing Conditions [in:] LMEs of the World's Regional Seas, K. Sherman & G. Hempel (eds.), UNEP Regional Seas, Report and Studies.

Heileman, S., Lutjeharms, J.R.E., Scott, L.E.P., 2008. Red Sea, LME Report by the Oceanographic Res. Inst., Durban.

Hu, C., Lee, Z., Franz, B., 2012. Chlorophyll *a* algorithms for oligotrophic oceans: a novel approach based on three-band reflectance difference. J. Geophys. Res. Oceans 117 (C1), 25 pp., http://dx.doi.org/10.1029/2011jc007395.

Jiang, H., Farrar, J.T., Beardsley, R.C., Chen, R., Chen, C., 2009. Zonal surface wind jets across the Red Sea due to mountain gap forcing along both sides of the Red Sea. Geophys. Res. Lett. 36 (19), 1—6, http://dx.doi.org/10.1029/2009GL040008.

Kahru, M., Gille, S.T., Murtugudde, R., Strutton, P.G., Manzano-Sarabia, M., Wang, H., Mitchell, B.G., 2010. Global correlations between winds and ocean chlorophyll. J. Geophys. Res. Oceans 115 (C12), 11 pp., http://dx.doi.org/10.1029/2010jc006500.

Kämpf, J., Chapman, P., 2016. Upwelling Systems of the World: A Scientific Journey to the Most Productive Marine Ecosystems. Springer, 433 pp., http://dx.doi.org/10.1007/978-3-319-42524-5.

Kara, A.B., Rochford, P.A., Hurlburt, H.E., 2003. Mixed layer depth variability over the global ocean. J. Geophys. Res. Oceans 108 (C3), 15 pp., http://dx.doi.org/10.1029/2000jc000736.

Koblentz-Mishke, O.J., Volkovinsky, V.V., Kabanova, J.G., 1970. Plankton primary production of the world ocean. In: Wooster, W.S. (Ed.), Scientific Exploration of the South Pacific. Nat. Acad. Sci., Washington, D.C., 257 pp.

Labiosa, R.G., Arrigo, K.R., Genin, A., Monismith, S.G., van Dijken, G., 2003. The interplay between upwelling and deep convective mixing in determining the seasonal phytoplankton dynamics in the Gulf of Aqaba: evidence from SeaWiFS and MODIS. Limnol. Oceanogr. 48 (6), 2355—2368, http://dx.doi.org/10.4319/lo.2003.48.6.2355.

Langodan, S., Cavaleri, L., Viswanadhapalli, Y., Hoteit, I., 2014. The Red Sea: a natural laboratory for wind and wave modeling. J. Phys. Oceanogr. 44 (12), 3139—3159, http://dx.doi.org/10.1175/JPO-D-13-0242.1.

Large, W.G., Pond, S., 1981. Open ocean momentum flux measurements in moderate to strong winds. J. Phys. Oceanogr. 11 (3), 324—336, http://dx.doi.org/10.1175/1520-0485(1981)011<0324:OOMFMI>2.0.CO;2.

Levanon-Spanier, I., Padan, E., Reiss, Z., 1979. Primary production in a desert-enclosed sea — the Gulf of Elat (Aqaba), Red Sea. Deep Sea Res. A Oceanogr. Res. Pap. 26 (6), 673—685, http://dx.doi.org/10.1016/0198-0149(79)90040-2.

Li, J., Wang, D., Chen, J., Yang, L., 2012. Comparison of remote sensing data with in-situ wind observation during the development of the South China Sea monsoon. Chin. J. Oceanol. Limnol. 30 (3), 933–943, http://dx.doi.org/10.1007/s00343-012-1285-6.

Lindell, D., Post, A.F., 1995. Ultraphytoplankton succession is triggered by deep winter mixing in the Gulf of Aqaba (Eilat), Red Sea. Limnol. Oceanogr. 40 (6), 1130–1141, http://dx.doi.org/10.4319/lo.1995.40.6.1130.

Loya, Y., Genin, A., el-Zibdeh, M., Naumann, M.S., Wild, C., 2014. Reviewing the status of coral reef ecology of the Red Sea: key topics and relevant research. Coral Reefs 33 (4), 1179–1180, http://dx.doi.org/10.1007/s00338-014-1170-1.

Maritorena, S., O'Reilly, J.E., 2000. OC2v2: update on the initial operational SeaWiFS chlorophyll *a* algorithm. NASA Tech. Memo. 2000-206892, vol. 11. NASA Goddard Space Flight Center, Greenbelt, Maryland, 3–8.

Marullo, S., Santoleri, R., Malanotte-Rizzoli, P., Bergamasco, A., 1999. The sea surface temperature field in the Eastern Mediterranean from advanced very high resolution radiometer (AVHRR) data: Part II. Interannual variability. J. Mar. Syst. 20 (1), 83–112, http://dx.doi.org/10.1016/S0924-7963(98)00072-4.

Marullo, S., Nardelli, B.B., Guarracino, M., Santoleri, R., 2007. Observing the Mediterranean Sea from space: 21 years of Pathfinder-AVHRR sea surface temperatures (1985 to 2005): re-analysis and validation. Ocean Sci. 3 (2), 299–310, http://dx.doi.org/10.5194/os-3-299-2007.

McWilliams, J.P., Côté, I.M., Gill, J.A., Sutherland, W.J., Watkinson, A.R., 2005. Accelerating impacts of temperature-induced coral bleaching in the Caribbean. Ecology 86 (8), 2055–2060, http://dx.doi.org/10.1890/04-1657.

Morcos, S.A., 1970. Physical and chemical oceanography of the Red Sea. Ocean. Mar. Biol. Ann. Rev. 8, 73–202.

Nykjaer, L., 2009. Mediterranean Sea surface warming 1985–2006. Clim. Res. 39 (1), 11–17, http://dx.doi.org/10.3354/cr00794.

Ocean Biology Processing Group, 2003. MODIS Aqua Level 3 Global Daily Mapped 4km Chlorophyll *a*. Ver. 6. PO.DAAC, CA, USA. (accessed 01.09.15).

Omstedt, A., 2011. Guide to Process Based Modeling of Lakes and Coastal Seas. Springer Science & Business Media, 258 pp., http://dx.doi.org/10.1007/978-3-642-17728-6.

Ouyang, Y., 2005. Evaluation of river water quality monitoring stations by principal component analysis. Water Res. 39 (12), 2621–2635, http://dx.doi.org/10.1016/j.watres.2005.04.024.

Papadopoulos, V.P., Abualnaja, Y., Josey, S.A., Bower, A., Raitsos, D. E., Kontoyiannis, H., Hoteit, I., 2013. Atmospheric forcing of the winter air–sea heat fluxes over the northern Red Sea. J. Clim. 26 (5), 1685–1701, http://dx.doi.org/10.1175/JCLI-D-12-00267.1.

Patzert, W.C., 1974. Wind-induced reversal in Red Sea circulation. Deep Sea Res. Oceanogr. Abstr. 21 (2), 109–121, http://dx.doi.org/10.1016/0011-7471(74)90068-0.

Pedgley, D.E., 1974. An Outline of the Weather and Climate of the Red Sea. L'oceanographie Phys. la Mer Rouge. CNEXO, Paris, 9–27.

Persson, A., 2011. User Guide to ECMWF Forecast Products. ECMWF, 129 pp.

Pickard, G.L., Emery, W.J., 1990. Descriptive Physical Oceanography: An Introduction. Elsevier, 320 pp., http://dx.doi.org/10.1016/c2009-0-11176-5.

Pickett, M.H., Tang, W., Rosenfeld, L.K., Wash, C.H., 2003. QuikSCAT satellite comparisons with nearshore buoy wind data off the US west coast. J. Atmos. Ocean. Technol. 20 (12), 1869–1879, http://dx.doi.org/10.1175/1520-0426(2003)020<1869:QSCWNB>2.0.CO;2.

Raitsos, D.E., Hoteit, I., Prihartato, P.K., Chronis, T., Triantafyllou, G., Abualnaja, Y., Release, E.O., Hole, W., Hole, W., Sciences, A., Carolina, N., Hole, W., Hole, W., 2011. Abrupt warming of the Red Sea. Geophys. Res. Lett. 38 (14), 1410–1425.

Raitsos, D.E., Pradhan, Y., Brewin, R.J.W., Stenchikov, G., Hoteit, I., 2013. Remote sensing the phytoplankton seasonal succession of the Red Sea. PLoS ONE 8 (6), e64909, http://dx.doi.org/10.1371/journal.pone.0064909.

Rao, N.V.N.D., Behairy, A.K.A., 1986. Nature and composition of shore-zone sediments between Jeddah and Yanbu, eastern Red Sea. Mar. Geol. 70 (3), 287–305, http://dx.doi.org/10.1016/0025-3227(86)90006-X.

Rasul, N.M.A., Stewart, I.C.F., 2015. The Red Sea: The Formation, Morphology, Oceanography and Environment of a Young Ocean Basin. Springer, 353 pp., http://dx.doi.org/10.1007/978-3-662-45201-1.

Reynolds, R.W., Smith, T.M., Liu, C., Chelton, D.B., Casey, K.S., Schlax, M.G., 2007. Daily high-resolution-blended analyses for sea surface temperature. J. Clim. 20 (22), 5473–5496, http://dx.doi.org/10.1175/2007JCLI1824.1.

Ricciardulli, L., Wentz, F.J., Smith, D.K., 2011. Remote Sensing Systems QuikSCAT Ku-2011 [Monthly] Orbital Swath Ocean Vector Winds L2B, Version 4. Remote Sensing Systems, Santa Rosa, CA, Available at: www.remss.com/missions/qscat (accessed 01.09.15).

Roberts, J.J., Best, B.D., Dunn, D.C., Treml, E.A., Halpin, P.N., 2010. Marine Geospatial Ecology Tools: an integrated framework for ecological geoprocessing with ArcGIS, Python, R, MATLAB, and C++. Environ. Model. Softw. 25 (10), 1197–1207, http://dx.doi.org/10.1016/j.envsoft.2010.03.029.

Samelson, R.M., Skyllingstad, E.D., Chelton, D.B., Esbensen, S.K., O'Neill, L.W., Thum, N., 2006. On the coupling of wind stress and sea surface temperature. J. Clim. 19 (8), 1557–1566, http://dx.doi.org/10.1175/JCLI3682.1.

Sarhan, T., García, J., Vargas, M., Vargas, J.M., Plaza, F., et al., 2000. Upwelling mechanisms in the northwestern Alboran Sea. J. Mar. Syst. 23 (4), 317–331, http://dx.doi.org/10.1016/S0924-7963(99)00068-8.

Shaltout, M., Omstedt, A., 2014. Recent sea surface temperature trends and future scenarios for the Mediterranean Sea. Oceanologia 56 (3), 411–443, http://dx.doi.org/10.5697/oc.56-3.411.

Shaltout, M., El Gindy, A., Omstedt, A., 2013. Recent climate trends and future scenarios along the Egyptian Mediterranean coast. Geofizika 30 (1), 19–41.

Shamsudduha, M., Chandler, R.E., Taylor, R.G., Ahmed, K.M., 2009. Recent trends in groundwater levels in a highly seasonal hydrological system: the Ganges–Brahmaputra–Meghna Delta. Hydrol. Earth Syst. Sci. 13 (12), 2373–2385, http://dx.doi.org/10.5194/hess-13-2373-2009.

Skliris, N., Sofianos, S., Gkanasos, A., Mantziafou, A., Vervatis, V., Axaopoulos, P., Lascaratos, A., 2012. Decadal scale variability of sea surface temperature in the Mediterranean Sea in relation to atmospheric variability. Ocean Dyn. 62 (1), 13–30, http://dx.doi.org/10.1007/s10236-011-0493-5.

Sofianos, S.S., 2003. An Oceanic General Circulation Model (OGCM) investigation of the Red Sea circulation: 2. Three-dimensional circulation in the Red Sea. J. Geophys. Res. 108 (C3), 3066, http://dx.doi.org/10.1029/2001JC001185.

Sofianos, S.S., Johns, W.E., 2003. An oceanic general circulation model (OGCM) investigation of the Red Sea circulation: 2. Three-dimensional circulation in the Red Sea. J. Geophys. Res. Oceans 108 (C3), 15 pp., http://dx.doi.org/10.1029/2001jc001185.

Sofianos, S.S., Johns, W.E., 2007. Observations of the summer Red Sea circulation. J. Geophys. Res. 112 (C6), C06025, http://dx.doi.org/10.1029/2006JC003886.

Sofianos, S.S.S., Johns, W.E.E., Murray, S.P.P., 2002. Heat and freshwater budgets in the Red Sea from direct observations at Bab el Mandeb. Deep Sea Res. Pt. II: Top. Stud. Oceanogr. 49 (7), 1323–1340, http://dx.doi.org/10.1016/S0967-0645(01)00164-3.

Stambler, N., 2005. Bio-optical properties of the northern Red Sea and the Gulf of Eilat (Aqaba) during winter 1999. J. Sea Res. 54 (3), 186–203, http://dx.doi.org/10.1016/j.seares.2005.04.006.

Tang, D., Kawamura, H., Luis, A.J., 2002. Short-term variability of phytoplankton blooms associated with a cold eddy in the northwestern Arabian Sea. Remote Sens. Environ. 81 (1), 82—89, http://dx.doi.org/10.1016/S0034-4257(01)00334-0.

Tong, J., Gan, Z., Qi, Y., Mao, Q., 2010. Predicted positions of tidal fronts in continental shelf of South China Sea. J. Mar. Syst. 82 (3), 145—153, http://dx.doi.org/10.1016/j.jmarsys.2010.04.011.

Trenberth, K.E., Large, W.G., Olson, J.G., 1990. The mean annual cycle in global ocean wind stress. J. Phys. Oceanogr. 20 (11), 1742—1760, http://dx.doi.org/10.1175/1520-0485(1990)020<1742:TMACIG>2.0.CO;2.

Triantafyllou, G., Yao, F., Petihakis, G., Tsiaras, K.P., Raitsos, D.E., Hoteit, I., 2014. Exploring the Red Sea seasonal ecosystem functioning using a three-dimensional biophysical model. J. Geophys. Res. Oceans 119 (3), 1791—1811, http://dx.doi.org/10.1002/2013JC009641.

Williams, R.G., Follows, M.J., 2011. Ocean Dynamics and the Carbon Cycle: Principles and Mechanisms. Cambridge University Press, 316—324, http://dx.doi.org/10.1017/cbo9780511977817.010.

Wold, S., Esbensen, K., Geladi, P., 1987. Principal component analysis. Chemom. Intell. Lab. Syst. 2 (1—3), 37—52, http://dx.doi.org/10.1016/0169-7439(87)80084-9.

Yao, F., Hoteit, I., Pratt, L.J., Bower, A.S., Köhl, A., Gopalakrishnan, G., Rivas, D., 2014. Seasonal overturning circulation in the Red Sea: 2. Winter circulation. J. Geophys. Res. Oceans 119 (4), 2263—2289, http://dx.doi.org/10.1002/2013JC009331.

Zhai, P., Bower, A.S., Smethie, W.M., Pratt, L.J., 2015. Formation and spreading of Red Sea Outflow Water in the Red Sea. J. Geophys. Res. Oceans 120 (9), 6542—6563, http://dx.doi.org/10.1002/2015JC010751.

Zhan, P., Subramanian, A.C., Yao, F., Hoteit, I., 2014. Eddies in the Red Sea: a statistical and dynamical study. J. Geophys. Res. Oceans 119 (6), 3909—3925, http://dx.doi.org/10.1002/2013jc009563.

Zhan, P., Subramanian, A.C., Yao, F., Kartadikaria, A.R., Guo, D., Hoteit, I., 2016. The eddy kinetic energy budget in the Red Sea. J. Geophys. Res. Oceans 121 (7), 4732—4747, http://dx.doi.org/10.1002/2015jc011589.